

**DESIGN OF A SOFT GRIPPER FOR PICK AND PLACE
APPLICATION**

LOW MUN SENG

**A project report submitted in partial fulfilment of the
requirements for the award of Bachelor of Engineering
(Honours) Electrical and Electronic Engineering**

**Lee Kong Chian Faculty of Engineering and Science
Universiti Tunku Abdul Rahman**

Jan 2021

DECLARATION

I hereby declare that this project report is based on my original work except for citations and quotations which have been duly acknowledged. I also declare that it has not been previously and concurrently submitted for any other degree or award at UTAR or other institutions.

Signature : Mun Seng

Name : LOW MUN SENG

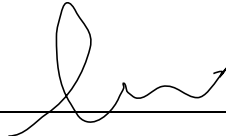
ID No. : 1704314

Date : 3 May 2021

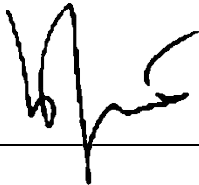
APPROVAL FOR SUBMISSION

I certify that this project report entitled “**DESIGN OF A SOFT GRIPPER FOR PICK AND PLACE APPLICATION**” was prepared by **LOW MUN SENG** has met the required standard for submission in partial fulfilment of the requirements for the award of Bachelor of Engineering (Honours) Electrical and Electronic Engineering at Universiti Tunku Abdul Rahman.

Approved by,

Signature : 

Supervisor : Dr. Chee Pei Song
Date : 3 May 2021

Signature : 

Co-Supervisor : Prof. Ts. Dr. Lim Eng Hock
Date : 3 May 2021

The copyright of this report belongs to the author under the terms of the copyright Act 1987 as qualified by Intellectual Property Policy of Universiti Tunku Abdul Rahman. Due acknowledgement shall always be made of the use of any material contained in, or derived from, this report.

© 2021, Low Mun Seng. All right reserved.

ACKNOWLEDGEMENTS

I would like to take this opportunity to thank everyone who has contributed to the successful completion of this project. This project would not be a success without help from you all.

First of all, I would like to express my gratitude to my Final Year Project supervisor, Dr. Chee Pei Song for his invaluable patience and guidance throughout the journey of conducting this project. He always provides me with useful ideas and suggestions whenever I faced any problems. His guidance throughout the journey helped me understand my project better so that I can achieve beyond my targeted goals.

Besides, I would also like to thank my co-supervisor, Prof. Ts. Dr. Lim Eng Hock for his guidance and support. In addition, I would like to express my gratitude to my loving parents, seniors (Mr. Low Jen Hahn and Mr. Goh Qi Lun) and friends who had helped and given me encouragement throughout the entire process.

ABSTRACT

Soft Robotic Gripper (SRG) emerges as a new member of the robotic family whereby it offers promising features, such as being lightweight, low cost, soft, highly compliant, easy to fabricate, and simple to control. Due to these amazing features, SRG has become one of the most promising technologies for pick and place applications in several industries, ranging from biomedical to the food industry. However, research about current SRG only focused on one of the many parameters that would affect the overall performance. A thorough theoretical understanding of how the structural parameters affect the overall performance is still missing. Besides, there is no suitable sensor available in the market as the conventional rigid sensor is not suitable for this highly compliant gripper. Therefore, the purpose of this study is to consider all contributing parameters that would affect the performance of the SRG, such as shape, length, thickness, gap shape, gap distance, and volume of the air chamber. In addition, a soft sensor based on Triboelectric Nanogenerator (TENG) mechanisms will be introduced. The parametric studies were conducted using Abaqus CAE simulation software and SolidWorks. Ecoflex 00-50 was used to fabricate the soft pneumatic actuator (SPA) and the sponge-like TENG sensor based on single electrode mode. A linear actuator attached with a syringe was used to provide pneumatic pressure to the SRG to perform pick and place applications. An improved SPA design with an extruded semi-cylinder between the SPA gap and additional 2.5 mm semi-cylindrical air chamber was proposed based on the results obtained from the parametric studies with 0.9258% performance higher than the conventional design. Next, the fabricated sponge-like TENG sensor has provided a unique peak voltage for each material and item. The obtained results allowed this project to be further extended to performing an object-recognition system enhanced with machine learning features. Lastly, the results suggested the improved SPA with a unique character is able to perform pick and place applications, and the fabricated sponge-like TENG sensor is feasible to be implemented to the SRG.

TABLE OF CONTENTS

DECLARATION		ii
APPROVAL FOR SUBMISSION		iii
ACKNOWLEDGEMENTS		v
ABSTRACT		vi
TABLE OF CONTENTS		vii
LIST OF TABLES		ix
LIST OF FIGURES		x
LIST OF SYMBOLS / ABBREVIATIONS		xiii
LIST OF APPENDICES		xiv
CHAPTER		
1	INTRODUCTION	1
1.1	General Introduction	1
1.2	Importance of the Study	2
1.3	Problem Statement	2
1.4	Aim and Objectives	3
1.5	Scope and Limitation of the Study	3
1.6	Contribution of the Study	4
1.7	Outline of the Report	4
2	LITERATURE REVIEW	5
2.1	Introduction	5
2.2	Design of the Soft Gripper	5
2.2.1	The Shape of the Finger	5
2.2.2	The Length of the Finger	6
2.2.3	The Thickness of the Finger	7
2.2.4	The Material of the Finger	9
2.3	Fabricating Methods	10
2.3.1	Casting Method	10
2.3.2	3D Printing Method	12

2.4	Control System for the Soft Robotic Gripper	13
2.4.1	Inflate and Deflate	13
2.4.2	Microcontrollers	15
2.5	Triboelectric Nanogenerator, TENG	17
2.5.1	Introduction	17
2.5.2	Working Principles	18
2.5.3	Design of the Sensor	21
3	METHODOLOGY AND WORK PLAN	24
3.1	Introduction	24
3.2	Design of SPA using SolidWorks	25
3.3	Abaqus CAE Simulation	26
3.4	SRG Fabrication Process	28
3.4.1	Mould and SPA Holder Design	28
3.4.2	Fabrication of SPA	30
3.4.3	Soft Robotic Gripper, SRG	31
3.5	Control System	32
3.6	Fabrication of TENG Sensor	36
4	RESULTS AND DISCUSSION	38
4.1	Introduction	38
4.2	Simulation and Experimental Results	38
4.2.1	Study on SPA Gap Distance	38
4.2.2	Study on SPA Air Chamber Volume	40
4.2.3	Study on SPA Gap Shape	41
4.2.4	Improved SPA	42
4.3	Hardware Features	46
4.4	TENG Sensor	48
5	CONCLUSIONS AND RECOMMENDATIONS	50
5.1	Conclusions	50
5.2	Recommendations for Future Work	50
	REFERENCES	52
	APPENDICES	56

LIST OF TABLES

Table 3.1: System and Equipment Requirements	33
Table 3.2: System Specifications	33

LIST OF FIGURES

Figure 2.1: Design of the SPA	5
Figure 2.2: Pull-off Force Against Diameter of the Sphere	6
Figure 2.3: Force-displacement Characteristics of Bending SPA Samples with Different Wall Thicknesses	8
Figure 2.4: The Directionality of the Curvature in Actuated PneuNets	8
Figure 2.5: Bending Angle of Actuator with Different Materials	9
Figure 2.6: Block Diagram of Multi-step Moulding Process	11
Figure 2.7: Fabrication Process of a Single Soft Finger	11
Figure 2.8: Schematic of Bottom-up DLP Printing Process	12
Figure 2.9: Flowchart of 3D Printing Process	13
Figure 2.10: Bending of SPA at Different Input Pressure	13
Figure 2.11: Experimental Setup for Investigating the Curling Actuator	14
Figure 2.12: Pneumatic Circuit Diagram	15
Figure 2.13: Arduino UNO R3	15
Figure 2.14: Arduino Specifications	16
Figure 2.15: ESP32 Diagram	16
Figure 2.16: ESP32 Specification	17
Figure 2.17: Four Fundamental Modes of Triboelectric Nanogenerators	18
Figure 2.18: Schematic Diagram of the Sensor	19
Figure 2.19: Triboelectric Skin	20
Figure 2.20: Tribo-skin Working Mechanism	20
Figure 2.21: Fabrication Process of the SS-TENG sensor	21
Figure 2.22: Working Principles of SS-TENG sensor	22
Figure 2.23: Corresponding Open-circuit Voltage under Different Forces	22

Figure 3.1: Overall Project Flow for an SRG System	24
Figure 3.2: Flowchart of Designing the SPA	25
Figure 3.3: (a) Conventional and (b) Improved SPA Sketched in SolidWorks	25
Figure 3.4: Abaqus CAE Simulation Process	26
Figure 3.5: User Interface of Abaqus CAE	27
Figure 3.6: Simulated Bending Angle Measured using 3 Nodes in Abaqus CAE	28
Figure 3.7: Block Diagram for Mould Design	29
Figure 3.8: Conventional SPA Moulds (left) and Improved SPA Moulds (Right)	29
Figure 3.9: 3D Printed Moulds for Conventional (left) and Improved (right) SPA	29
Figure 3.10: SPA Holder Sketch (left) and 3D Printed SPA Holder (right)	30
Figure 3.11: SPA Fabrication Process	30
Figure 3.12: (a) Lower Layer, (b) Upper Layer, and (c) Fabricated SPA	31
Figure 3.13: An SRG with 3 SPAs connected to Oxygen Nasal Cannula	31
Figure 3.14: Hardware Circuit	34
Figure 3.15: Overall Flowchart of the System	35
Figure 3.16: Flowchart of the Pressure Sensor	35
Figure 3.17: Hardware Prototype Attached with a 200 ml Syringe	36
Figure 3.18: Fabrication of Sponge-like TENG Sensor.	36
Figure 3.19: SPA Attached with a Sponge-like TENG Sensor	37
Figure 4.1: Bending Angle of Different Gap Distance	39
Figure 4.2: Comparison between 2 mm (green) and 8 mm (red) Gap Distance	40
Figure 4.3: Bending Angle of Different Air Chamber Volume	40
Figure 4.4: Design of SPA Gap Shape	41

Figure 4.5: Bending Angle of Different Gap Shape (Extruded Cut)	41
Figure 4.6: Bending Angle of Different Gap Shape (Extruded)	42
Figure 4.7: Additional Semi-cylindrical Air Chamber	43
Figure 4.8: Bending Angle of Different Diameter of the Semi-cylindrical Air Chamber	43
Figure 4.9: Comparison between Conventional SPA and Improved SPA	44
Figure 4.10: Comparison between Conventional SPA (red) and Improved SPA (green)	44
Figure 4.11: Simulation Results and Experimental Results	45
Figure 4.12: Comparison between Simulation Results and Experimental Results of Improved SPA	46
Figure 4.13: Deflated (left) and Inflated (right)	47
Figure 4.14: SRG Grabbing Different Objects (a)Aluminium Can, (b)Sphere, (c)Rectangle Box, and (d)Cylindrical Bottle	47
Figure 4.15: OLED Status	48
Figure 4.16: Generated V_{peak} by Sponge-like TENG Sensor	48

LIST OF SYMBOLS / ABBREVIATIONS

α	bending angle, °
V_{peak}	Peak Voltage, V
DLP	Digital Light Processing
IDE	Integrated Development Environment
I/O	Input/Output
SPA	Soft Pneumatic Actuator
SRG	Soft Robotic Gripper
SS-TENG	Sponge-like Silicone-based Triboelectric Nanogenerator
TENG	Triboelectric Nanogenerator

LIST OF APPENDICES

APPENDIX A: Fabrication Process of SPA	56
APPENDIX B: Fabrication Process of SPA	56
APPENDIX C: Fabrication Process of SPA	56
APPENDIX D: Pneumatic Circuit Diagram	57
APPENDIX E: Pinout Diagram of Arduino UNO R3	57
APPENDIX F: Pinout Diagram of ESP32	58
APPENDIX G: Design of all SPA	58
APPENDIX H: Pressure Table Generated by MPX5500DP	62
APPENDIX I: Triboelectric Series	63
APPENDIX J: Arduino Code (Main Program)	64
APPENDIX K: Arduino Code (MPX5500DP Pressure Sensor)	67

CHAPTER 1

INTRODUCTION

1.1 General Introduction

Soft robotic gripper (SRG) emerge as an additional new member of the robotic family that offers few promising features: lightweight, low cost, soft, highly compliant, easy to fabricate, and simple to control (Hao et al., 2016). This new member is different from the conventional hard grippers due to their compliance and safety (Li et al., 2020). Now, SRG has become one of the most promising technologies in pick and place applications due to the features mentioned above compared to the conventional rigid grippers that are heavy, hard, and have a limited degree of freedom (Salem et al., 2018).

The SRG can be used for pick and place applications, especially in gripping soft and fragile items. It would be more suitable to use a soft gripper instead of a hard gripper to grab soft items in the food packaging industry or to grab batteries in the automation industry. This is because the conventional gripper fails to differentiate the unique shape and characteristics of each targeted object (Wang, Or and Hirai, 2020).

There are several ways to actuate the SRG, and they can be categorised into three categories, variable-length tendon, fluidic actuation, and intelligent material actuation (Li et al., 2020). There are two sub-categories under fluidic actuation, which are pneumatic and hydraulic to inflate or deflate the inner chambers of the soft gripper (Hao et al., 2016). Based on grasping principles, the SRG can be classified into three groups, gripping based on actuation, gripping depended on controlled stiffness, and gripping by controlled adhesion. The first group uses pneumatic to actuate the soft gripper as proposed in Li et al. (2020)'s research.

Besides, Yap, Ng and Yeow (2016) stated the SRG can be done using four methods: mould techniques, lost wax casting, retraction in casting and direct 3D printing with a bottom-up approach. Each technique has its pros and cons, but mould techniques and 3D printing are the preferred option by many researchers.

In this project, an SRG based on pneumatic actuation for pick and place applications will be discussed. The method of fabrication will be the classic method – mould techniques. In order to enhance the efficiency of the gripper, an improved SRG will be proposed based on the parametric studies, and a potential soft sensor will be introduced.

1.2 Importance of the Study

The main purpose of this project is to study the working principles of an SRG as it is blooming in many industries. The SRG may be implemented in many fields, such as biomedical, micro-electro-mechanical systems and robotics due to its promising features.

Besides, the design of a conventional SRG can be improved to boost up the overall performance. This is because the design of the SRG may have significant impacts on the bending angle. On the other hand, a soft sensor can be introduced to increase the accuracy of the gripper for pick and place applications. Therefore, this project may contribute to society and the industry by introducing a Triboelectric Nanogenerator (TENG) sensor based on TENG mechanisms to produce a self-power sponge-like TENG sensor for the highly compliant SRG.

1.3 Problem Statement

Although there are a lot of works and studies that have been done for SRG, most of them have been focused on the design of Soft Pneumatic Actuator (SPA), applications of the SRG or materials of the SPA but less focused on the parametric studies of the SPA. Even if there were studies about how the gripper's parameter affected overall performance, most of the studies were limited and only considered one of the many parameters. A thorough theoretical understanding of how the structural parameters affect the overall performance is still missing.

Besides, due to SRG's promising features, such as being highly compliant, the lack of a suitable sensor could be a problem. According to Li et al. (2019), the authors discussed the importance of designing a soft sensor that portrays great compliance so that it can be attached to the SRG. According to Adam Bilodeau, White and Kramer (2015), soft robots undergo high strains

during actuation; hence, the traditional rigid sensor fails to be integrated into the system. According to Zhu et al. (2020), the authors stated there is no suitable sensor for the SRG. Such a problem will cause the SRG to fail in achieving its maximum potential in practical applications. To date, designing a soft sensor for SRG remains a challenge to be overcome.

1.4 Aim and Objectives

The main objective of this project is to design a soft gripper for pick and place applications. The details of the objectives are listed below:

- i. To study the working principle of a soft robotic gripper.
- ii. To design and introduce a soft sensor for the soft robotic gripper.
- iii. To characterize the soft robotic gripper.

1.5 Scope and Limitation of the Study

There are some limitations of this study as described below,

Firstly, this project involves Ecoflex to fabricate the SPA. Different materials, such as Dragon-skin, Tango+ or AR-G1L could produce different outcomes. Therefore, the outcome of this project is merely based on the SPA which is fabricated using Ecoflex 00-50.

Besides, the pressure supplied to the SPA is limited by using a 200 ml syringe. The measurement of the pressure supplied is based on a pressure table built by a pressure sensor, MPX5500DP and a 200 ml syringe. Hence, the pressure reading might not be precise.

Lastly, the implementation of the TENG sensor is limited due to time constraint and wide scope. The output voltage of the TENG is measured by a multimeter instead of feeding it into a microcontroller. Only the peak voltages are recorded. Therefore, it could potentially affect the accuracy of the collected data.

1.6 Contribution of the Study

In this project, the parametric studies of the SRG will be examined thoroughly, and the novelty of soft sensor based on TENG mechanisms will be discussed.

The contributions of this project are listed below:

- i. Discuss how each parameter affects the SRG overall performance.
- ii. Discuss the fabrication methods of the SRG.
- iii. Discuss the method to control the gripper's motion.
- iv. Introduce a soft sensor.
- v. Characterize the SRG.

1.7 Outline of the Report

This report consists of five chapters. Each chapter will provide the readers with the adequate amount of information. Below are the descriptions of each chapter.

Chapter 1 will discuss the project details, objectives, aims, scope and limitation of the study and contribution of the study to allow the reader to have a basic understanding of the overall project.

Chapter 2 will discuss the research findings of related works that have been conducted previously. This chapter will provide the readers with the fundamental knowledge of SRG and TENG mechanisms.

Chapter 3 will explain the methods to perform the whole project. The readers will be able to reperform the project by following the procedures. The flow of the project is presented using flowcharts and diagrams to have better visualization and understanding.

Chapter 4 will show the findings of the project, such as simulation results, experimental results and hardware features. Each result will be explained and discussed thoroughly.

Chapter 5 will conclude this project and suggestions for any potential ideas that can further extend this project.

CHAPTER 2

LITERATURE REVIEW

2.1 Introduction

SRG has been introduced to the market for several years. To date, there are plenty of soft gripper designs and fabrication methods available in the market due to their favourable features. In this chapter, the design of soft robotic gripper, fabrication methods, control systems, and feedback systems will be discussed thoroughly based on the previous works done by other researchers.

2.2 Design of the Soft Gripper

The design of the soft gripper plays an important role as it will affect the efficiency and the bending angle of the SPA. Therefore, the design of the soft gripper should be taken into account in designing a soft gripper for pick and place applications.

2.2.1 The Shape of the Finger

According to Herianto et al. (2019), an SPA can be classified based on how they operate. For instance, thermal-driven, flexible shaft, pneumatic or electro-driven. For the pneumatic actuator, it is crucial to ensure the gripper will bend when pressure is supplied to the air chambers. Researchers also proposed three designs of the SPA, as shown in Figure 2.1.

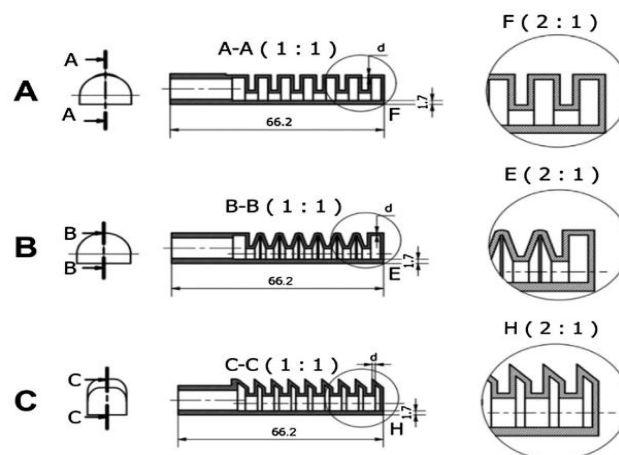


Figure 2.1: Design of the SPA (Herianto et al., 2019)

Based on the design A, B and C, the design of Model A is the most suitable as it bends the most followed by Model B and Model C when 400 kPa was supplied to the SPAs. The design of Model A is very common and is being used in multiple research papers, such as Wang, Or and Hirai (2020), Wang et al. (2018), Sun et al. (2020), Li et al. (2020), Salem et al. (2018) and Hao et al. (2016). This is because the design of Model A offers a great bending angle during inflation and an average bending angle during deflation. In comparison, the design of Model B would only offer a higher bending angle than Model A during deflation followed by Model C. Hence, the design of Model A is the conventional design as it offers an average performance during inflation and deflation.

2.2.2 The Length of the Finger

According to Hao et al. (2016), the gripper performance can be determined based on the “sweet” length of the gripper. An object with a smaller diameter would require a shorter effective length, while a larger diameter object would require a longer effective length. It can be concluded that the effective length is directly proportional to the diameter of the object. Therefore, choosing the right length for the gripper design plays a vital role as it would affect the gripper’s performance.

The maximum force generated during the whole gripping process is known as pull-off force, and the unit is newton (N). Figure 2.2 shows a line graph of pull-off force against the diameter of the sphere.

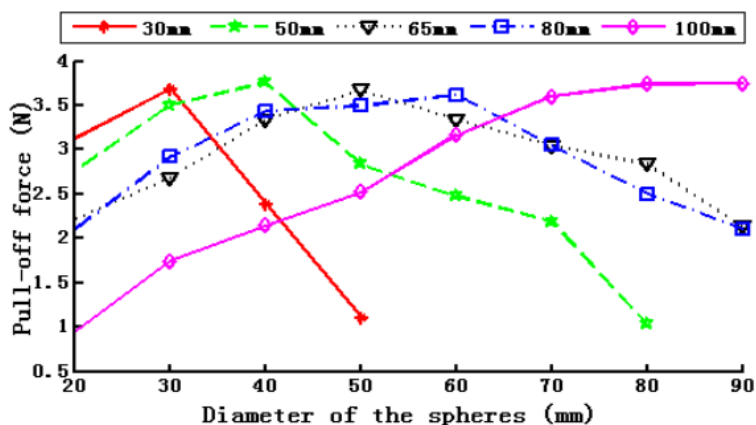


Figure 2.2: Pull-off Force Against Diameter of the Sphere (Hao et al., 2016)

The gripper with an effective length of 30 mm required approximately 3.75 N to grab a 30 mm diameter sphere whereas, it only required approximately 1 N to grab a 50 mm diameter sphere. This is because a gripper with a 30 mm effective length required more pressure to inflate the gripper to fully grab the 30 mm diameter sphere. Since the 50 mm diameter sphere is larger than the 30 mm gripper, it only required 1 N pressure to inflate the gripper to the maximum size. It can be expanded to grab the 50 mm diameter sphere. Based on the results, it can be concluded that the pull-off force will be the highest when the effective length is closed to the diameter of the object and decreased when the diameter of the object is larger than the effective length.

By selecting the appropriate effective length for the SRG, the pull-off force can be kept at a minimum. As a result, the power consumption can be reduced as lower pressure is required. Generally, a gripper with 100 mm effective length would be an ideal case as the pull-off force is relatively low for grabbing items with a diameter ranging from 20 to 50 mm.

2.2.3 The Thickness of the Finger

According to Sun, Song and Paik (2013), the wall thickness will affect the deformation of the gripper. This is because thicker walls will resist the gripper's deformation, and thinner walls will have lower resistance towards deformation of the gripper. When the resistance towards gripper's deformation is high, the gripper will tend to bend less as it has a lower force acting on the inner air chamber. Figure 2.3 shows the Force-displacement characteristics of bending SPA samples with different wall thicknesses.

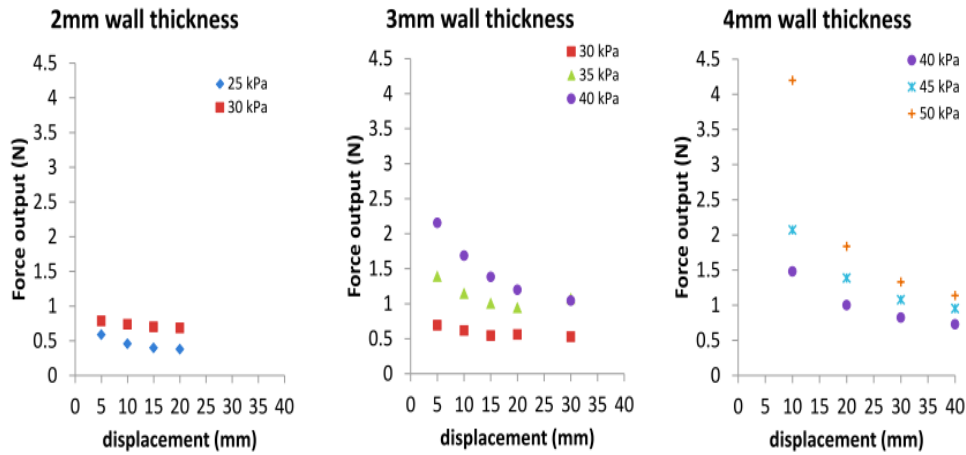


Figure 2.3: Force-displacement Characteristics of Bending SPA Samples with Different Wall Thicknesses (Sun, Song and Paik, 2013)

Based on Figure 2.3, the SPA with 2 mm wall thickness supplied with 30 kPa pneumatic pressure can produce 0.79 N force output. Compared to 3mm wall thickness with the same amount of supplied pressure, it can only produce a 0.69 N force output. Similar to 3 mm and 4 mm wall thickness supplied with 40 kPa. The generated force output was 2.15 N and 1.48 N for 3 mm and 4 mm wall thickness, respectively. The results suggested that a thicker wall will cause the SPA to bend less and generate a lower force output.

As discussed earlier, the gripper with a thinner wall will have lower resistance towards deformation. This is because when the gripper is pressurized, the channels will expand in the most compliant region, also known as the area with the lowest resistance to stretching. Figure 2.4 shows a diagram to illustrate the phenomena.

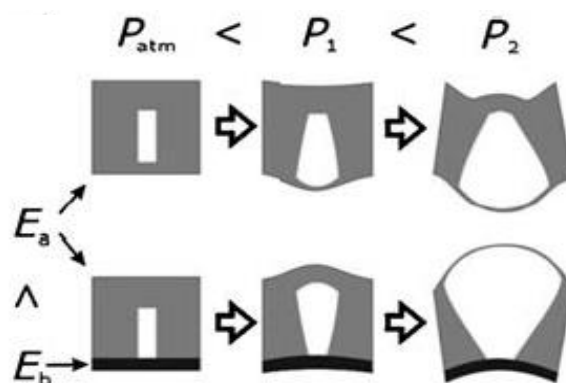


Figure 2.4: The Directionality of the Curvature in Actuated PneuNets (Ilievski et al., 2011)

The wall with the lowest stiffness will get thinner and expand due to the high compliance when pneumatic pressure is supplied. At the same time, the wall with the highest stiffness will act as a backbone and provide a concave bending shape (Ilievski et al., 2011).

2.2.4 The Material of the Finger

Currently, the most common material used to fabricate the SPA is Ecoflex. However, different materials could be used instead of Ecoflex to achieve different outcomes. Wang et al. (2018) proposed using Dragon-skin, Tango+, and AR-G1L to study the bending angles generated by the different SPA with different materials. Figure 2.5 shows the bending angle of SPA with different materials.

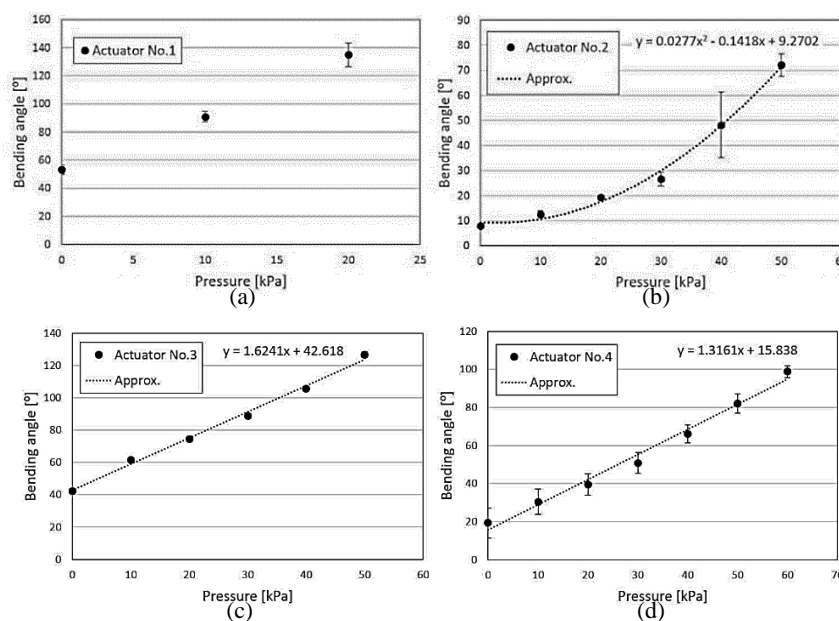


Figure 2.5: Bending Angle of Actuator with Different Materials (Wang et al., 2018)

Based on Figure 2.5, (a) Dragon-skin, (b) Dragon-skin coated with Ecoflex, (c) Tango+, and (d) AR-G1L are arranged according to the softness of the material such that (a) is the softest and (d) is the hardest. As shown in Figure 2.5 (a), it has provided the highest bending angle because Dragon-skin is the softest material as compared to others. Due to it being the softest, it required lower pneumatic pressure to achieve a high bending angle. Comparing (a) and

(d), (a) only required 20 kPa pneumatic pressure to achieve the bending angle of approximately 135° while (d) only managed to achieve the bending angle of approximately 100° with 60 kPa of pneumatic pressure. The results suggest that the bending angle is directly proportional to the softness of the actuator.

Although SPA with softer materials can obtain a greater bending angle with lower pneumatic pressure, ultimately reducing the power consumption. However, consideration such as being not able to withstand high input pressure shall be considered.

Figure 2.5 (b) produces a non-linear graph due to having two different materials in a single SPA. When the soft actuator is fabricated using Dragon-skin and coated with Ecoflex, it will bend differently (uneven) and impose unbalanced grasping forces. This is not an ideal case and shall be avoided as SPA needs even grasping force to perform pick and place applications accurately and efficiently.

In short, different materials with different stiffness will produce different bending angle. Hence, understanding the characteristics of each material and selecting the right material for the right applications is important in designing the SPA.

2.3 Fabricating Methods

There are many fabricating methods to fabricate the SRG, such as 3D Printing, heat-sealing, and casting techniques (Li et al., 2020). The fabrication method is supported by Rus and Tolley (2015), as the authors mentioned the SRG could be fabricated using multi-material 3D printing, shape deposition manufacturing, and soft lithography. Shape deposition manufacturing is similar to the casting method, where both methods also required the use of moulds. In this subchapter, only the casting method and 3D printing technique will be discussed in Chapter 2.3.1 and 2.3.2, respectively.

2.3.1 Casting Method

The casting method is the most classic technique to fabricate the SPA. Herianto et al. (2019) proposed a casting method that required multiple steps and an extra bonding process. The process can be simplified using a block diagram as shown

in Figure 2.6, and an example of how to fabricate an SPA is shown in Figure 2.7.



Figure 2.6: Block Diagram of Multi-step Moulding Process

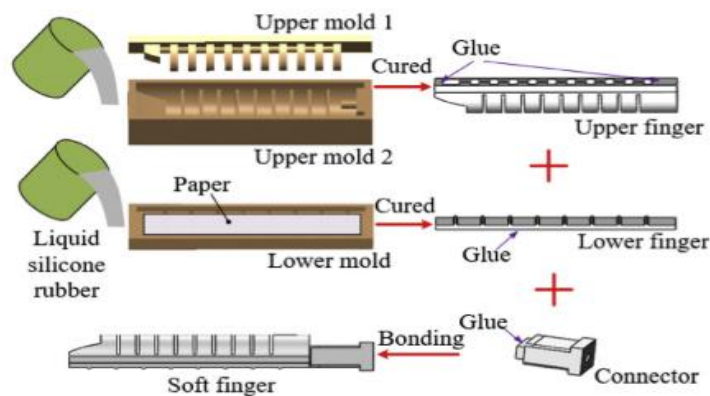


Figure 2.7: Fabrication Process of a Single Soft Finger (Zhong, Hou and Dou, 2019)

Based on Figure 2.7, the fabrication process can be summarized below

- 1) Silicon rubber liquid is mixed.
- 2) The liquid is poured into the upper mould and lower mould carefully to avoid any formation of bubbles.
- 3) Moulds are cured in a vacuum oven for 2 hours.
- 4) Moulds are removed from the vacuum oven and left to cool at room temperature.
- 5) The upper and lower cured fingers are removed from the mould.
- 6) The lower finger and upper finger are bonded together using glue (Sil-Poxy).
- 7) A connector is connected to the finger and sealed with glue (Sil-Poxy).

Other fabrication processes of SPA proposed by other researchers are attached in Appendix A, B and C.

2.3.2 3D Printing Method

Besides the casting method, the 3D printing method can also be used to fabricate the SPA. Despite there being only a few soft materials for a 3D printer to fabricate the SPA, this method is still feasible to be used if the properties of the materials are well understood (Lipson, 2014). According to Wang et al. (2017), 2 types of 3D printer, such as Object260Connex printer (Stratasys, Minnesota, United States) and Agillista printer (Keyence, Japan) can be used to 3D print the SPA.

3D printing of SPA can be achieved in few ways. For instance, selective laser sintering, fused deposition modelling, fuse filament fabrication, and digital light processing (DLP). The first three methods provide low resolution and surface quality, whereas DLP can produce better resolution and surface quality. This method solidified the liquid photocurable resin entirely layer by layer while printing. Figure 2.8 shows the schematic of the bottom-up DLP printing process, and Figure 2.9 shows the overall process of 3D printing an SPA (Ge et al., 2018).

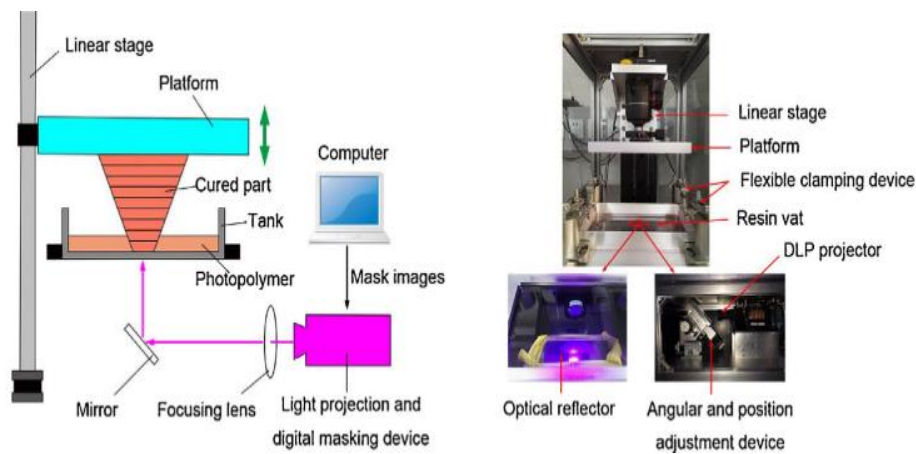


Figure 2.8: Schematic of Bottom-up DLP Printing Process (Ge et al., 2018)

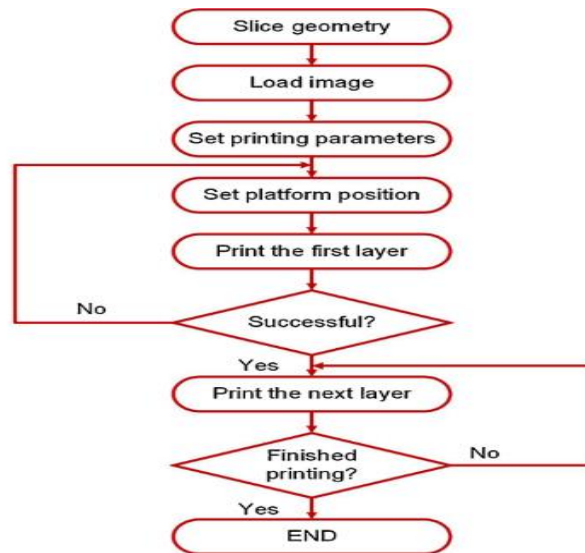


Figure 2.9: Flowchart of 3D Printing Process (Ge et al., 2018)

2.4 Control System for the Soft Robotic Gripper

A proper system to control the SRG plays a vital role in ensuring the SRG performs at its peak performance. Therefore, in this subchapter, the control system to inflate and deflate the SPA, and the microcontroller will be discussed thoroughly.

2.4.1 Inflate and Deflate

Since the SPA is based on pneumatic actuation, therefore, it required pneumatic pressure to inflate and deflate. Figure 2.10 shows an SPA bending at different level supplied pressure, and the α is indicating the bending angle.

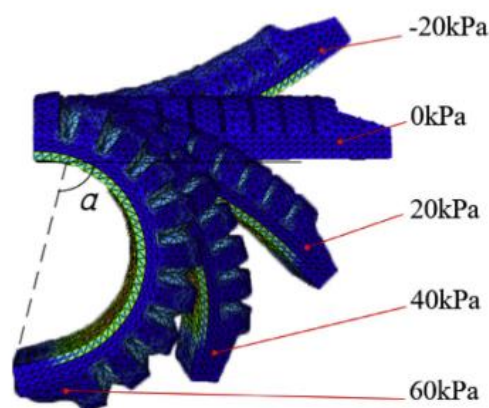


Figure 2.10: Bending of SPA at Different Input Pressure (Zhong, Hou and Dou, 2019)

Based on Figure 2.10, the bending of an SPA can be observed when pneumatic pressure is applied to the inner air chambers. When a negative input pressure is applied to the SPA, the finger will bend upward (deflate), whereas when a positive input pressure is applied to the SPA, the finger will curve downward (inflate). To achieve inflation and deflation of the finger, a system that can supply and vacuum air is needed to increase and decrease pressure inside the air chambers of the SPA.

As attached in Appendix D, the circuit diagram provided by Soft Robotic Toolkit can only provide positive pressure to the finger for inflation. However, there is no vacuum pump present in the proposed circuit. A vacuum pump is needed to provide negative pressure to the finger. Without the presence of a vacuum pump, the objective of this project will not be achieved. Therefore, the circuit diagram proposed by Soft Robotic Toolkit not being utilized. Figure 2.11 shows another circuit diagram proposed by researchers.

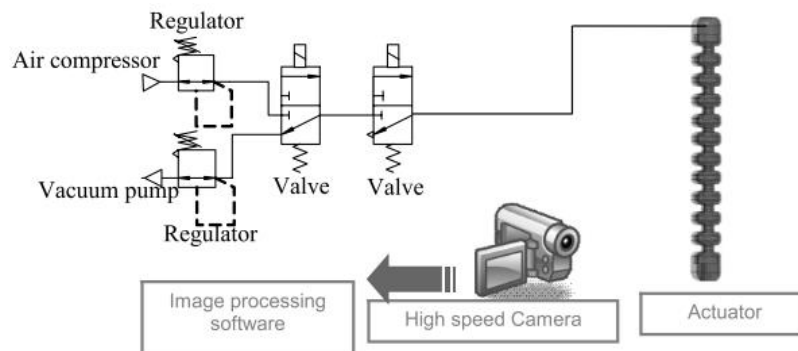


Figure 2.11: Experimental Setup for Investigating the Curling Actuator (Wakimoto, Suzumori and Ogura, 2011)

According to Wakimoto, Suzumori and Ogura (2011), they proposed a control system to investigate the displacement characteristic of the curling actuator. An air compressor and a vacuum pump are included to achieve inflation and deflation of the SPA by supplying positive and negative pneumatic pressure. However, there is a problem with the system, as shown in Figure 2.11. This vacuum pump will not connect to the actuator to reduce the pressure inside the air chambers due to the valve on the right side. A better system to inflate and deflate the SPA is proposed in Sun et al. (2020), as shown in Figure 2.12.

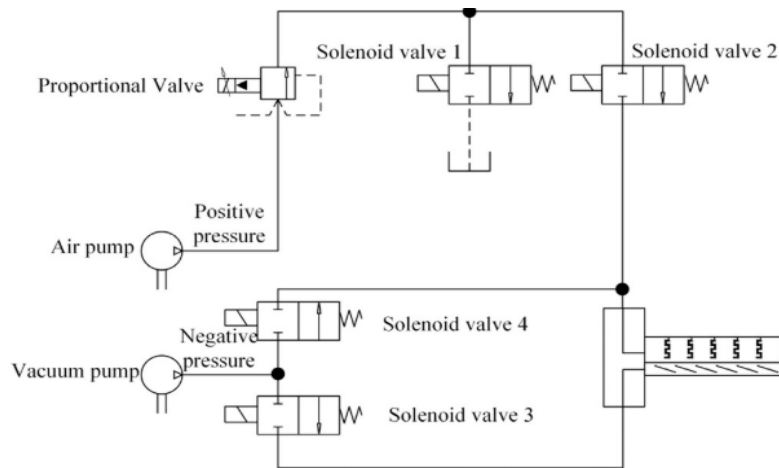


Figure 2.12: Pneumatic Circuit Diagram (Sun et al., 2020)

This proposed pneumatic circuit diagram is better as it can supply both positive and negative pressure into the air chambers of the actuator to inflate and deflate.

2.4.2 Microcontrollers

According to Badamasi (2014), a small microcontroller board with a USB plug to connect to a computer is Arduino. It is an inexpensive tool that provides users to write programming code using C or C++.

There are plenty of Arduino models available in the market, such as Arduino UNO, Nano, Due, and Mega, with different amount of Input/Output (I/O) pins. Figure 2.13 shows a diagram of Arduino UNO R3.



Figure 2.13: Arduino UNO R3 (Arduino, 2020)

Arduino UNO R3 is the most popular among the other models as it is cheap and powered by an Atmega 328 processor operating at 16 MHz. It also comes with 32 kB of Flash Memory, 1 kB of EEPROM, 2 kB of SRAM. The amount of I/O is also reasonable and sufficient such that it has 14 digital I/O, of which 6 provide PWM output. The specifications of Arduino UNO R3 is shown in Figure 2.14, and the pinout diagram is shown in Appendix E.

Microcontroller	ATmega328
Operating Voltage	5V
Input Voltage (recommended)	7-12V
Input Voltage (limits)	6-20V
Digital I/O Pins	14 (of which 6 provide PWM output)
Analog Input Pins	6
DC Current per I/O Pin	40 mA
DC Current for 3.3V Pin	50 mA
Flash Memory	32 KB of which 0.5 KB used by bootloader
SRAM	2 KB
EEPROM	1 KB
Clock Speed	16 MHz

Figure 2.14: Arduino Specifications (Arduino, 2020)

According to She et al. (2015), Arduino UNO R3 is used as the microcontroller to control the SRG. Besides, the sensor integrated into the system can be controlled using Arduino UNO R3 by feeding the output of the sensor as an input to the Arduino. However, there is an alternative option which is ESP32. It is a low-cost and low power microcontroller integrated with WiFi and dual-mode Bluetooth. It comes with 36 GPIOs and several features, such as ADC, DAC, and I2C, which are needed to control the SRG. Figure 2.15 shows the diagram of ESP32, and Figure 2.16 shows the specification of ESP32. The pinout diagram of ESP32 is shown in Appendix F.

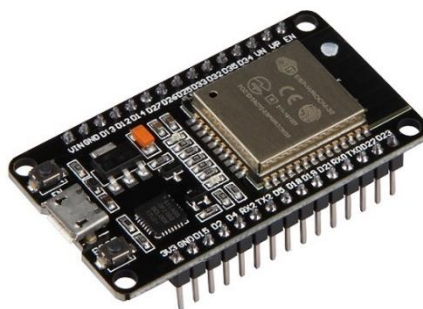


Figure 2.15: ESP32 Diagram (ESPRESSIF, n.d.)

Specifications – ESP32 DEVKIT V1 DOIT

Number of cores	2 (dual core)
Wi-Fi	2.4 GHz up to 150 Mbps/s
Bluetooth	BLE (Bluetooth Low Energy) and legacy Bluetooth
Architecture	32 bits
Clock frequency	Up to 240 MHz
RAM	512 KB
Pins	30 or 36 (depends on the model)
Peripherals	Capacitive touch, ADC (analog to digital converter), DAC (digital to analog converter), I2C (Inter-Integrated Circuit), UART (universal asynchronous receiver/transmitter), CAN 2.0 (Controller Area Network), SPI (Serial Peripheral Interface), I2S (Integrated Inter-IC Sound), RMII (Reduced Media-Independent Interface), PWM (pulse width modulation), and more.

Figure 2.16: ESP32 Specification (ESPRESSIF, n.d.)

ESP32 needs Arduino Integrated Development Environment (IDE), a free platform application that supports C programming language. IDE is used to write and upload the relevant codes to ESP32.

2.5 Triboelectric Nanogenerator, TENG

The purpose of studying Triboelectric Nanogenerator (TENG) is TENG becoming one of the hot topics in the current research field (Kim et al., 2020). The coupling effects between contact electrification and electrostatic induction of TENG allow the sensor to work independently without needing an external power source (Su et al., 2014). Such effect can be used to design a self-powered TENG sensor for several purposes, such as but not limited to the pressure sensor, tactile sensor, and bending sensor. In the following subchapters, an introduction of TENG will be discussed, followed by its working principles and the TENG sensor designed in previous research.

2.5.1 Introduction

TENG offers promising features, such as high output voltage and efficiency, low cost, versatility in structural design, great stability, robustness, and most importantly, being environmentally friendly (Wang, Lin and Wang, 2015). TENG can produce electricity when there is movement, such as touching, impact, vibration, etc. TENG operates based on triboelectrification and

electrostatic induction mechanisms producing electricity. Hence, the surface contact between the functional layers of the triboelectric device is the most important action during the operation. The functional layer is the layer with a material of either being the most negative affinity or positive affinity and the triboelectric response is directly proportional to the gap of the charge affinities between functional layers (Haque et al., 2018). There are four fundamental modes of TENG, as shown in Figure 2.17.

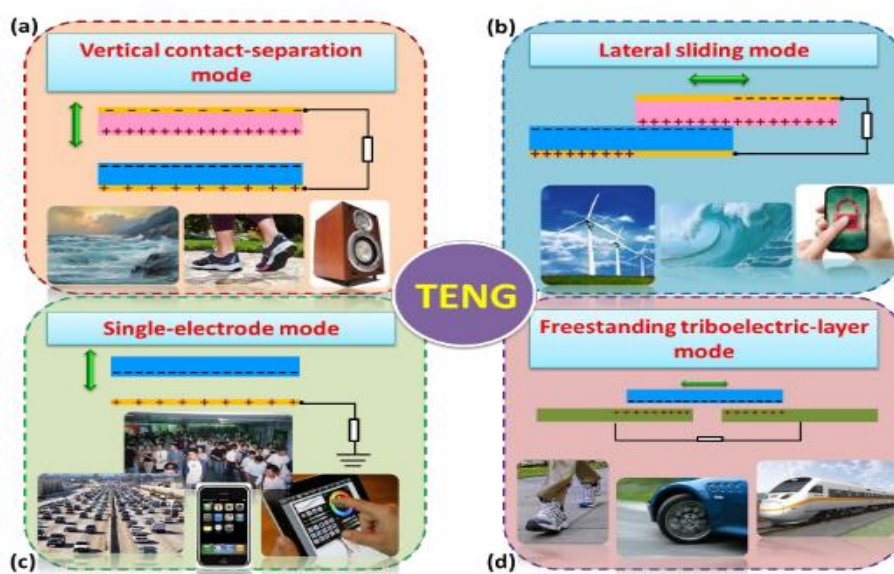


Figure 2.17: Four Fundamental Modes of Triboelectric Nanogenerators (Wang, Lin and Wang, 2015)

2.5.2 Working Principles

Vertical contact-separation mode and single-electrode mode are more common in developing a self-powered sensor for the SRG. Hence, only these two modes will be discussed in the following subchapters.

2.5.2.1 Vertical Contact-separation Mode

Vertical contact-separation mode required two different triboelectric polarities facing each other (negative and positive affinity). A conductive triboelectric layer at the negative affinity site act as an electrode. When there is movement, such as pressure force or mechanical force, the two functional layers will contact and allow an exchange of charges between functional layers. This phenomenon is known as contact electrification. When pressure force is no longer present,

the two functional layers will separate with a gap in the vertical-to-plane direction. This will trigger a change in electrical potential between layers, and the electrons will flow from the negative to positive affinity triboelectric later. When the pressure force is present again, it will cause contact electrification resulting in the triboelectric-charge-created potential being compensated and disappeared. At this moment, the flow of electrons back to achieve electrical equilibrium would occur (Wang, Lin and Wang, 2015 and Haque et al., 2018).

For this mode to achieve high performance, effective switching is required between the fully contacted state and fully separated state. Figure 2.18 shows a TENG sensor based on vertical contact-separation mode.

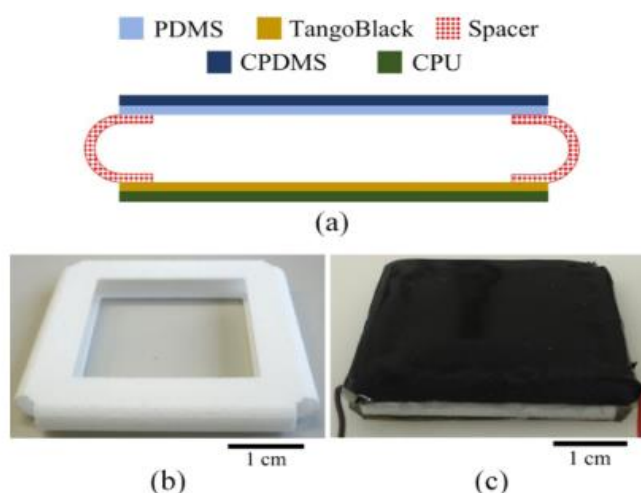


Figure 2.18: Schematic Diagram of the Sensor (Haque et al., 2018)

As discussed above, effective switching is important to achieve great performance. The spacer, as shown in Figure 2.18, plays an important role as a restoring mechanism during the operation. The height of the spacer is 5 mm, as after several trials and errors, 5 mm shows the greatest restoration results. Choosing the optimum height is important as when the height is too low, it will reduce the responses of the functional layers. On the other hand, when the height is too high, it will require a higher force to achieve contact electrification (Haque et al., 2018).

2.5.2.2 Single Electrode Mode

According to Wang, Lin and Wang (2015), any object with motion is usually charged due to its contact with air or other objects. These moving objects can be treated as a triboelectric layer in the TENG to produce electricity. Hence, the electrode can be reduced from two to one. This mode is known as the single-electrode mode. Unlike vertical-contact separation mode, this mode only includes one single electrode and another free moving object. Figure 2.19 shows a TENG sensor based on single-electrode mode.

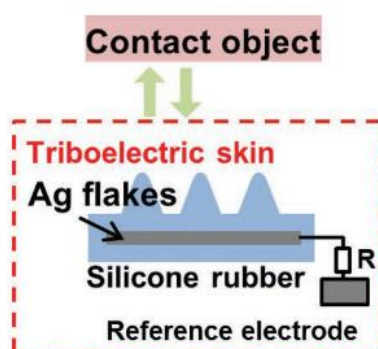


Figure 2.19: Triboelectric Skin (Lai et al., 2018)

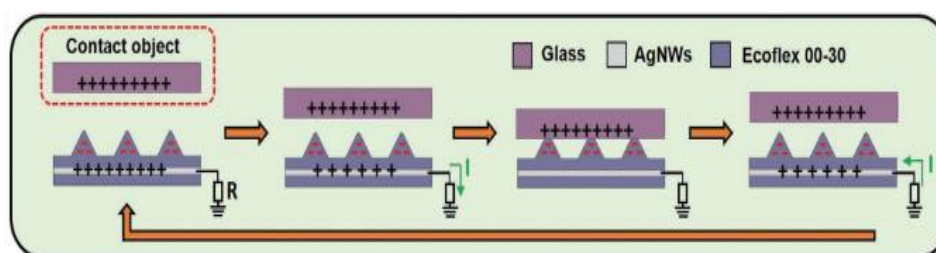


Figure 2.20: Tribo-skin Working Mechanism (Chen et al., 2020)

According to Figure 2.20, the generation of triboelectric is based on contact electrification and electrostatic induction. When an object comes in contact with the triboelectric skin, an exchange of charges between functional layers will occur. When the object is leaving the triboelectric skin, the gap between the two surfaces will increase, thus, creating a potential difference. The unscreened negative charges on the surface will prompt the flow of electrons from the silver flakes embedded in the triboelectric skin to the ground. This will induce the accumulation of positive charges in the electrodes and in the end,

will generate voltage. As the object continued moving away from the triboelectric skin's surface, electrical equilibrium is established. When the object is approaching the surface of the triboelectric skin, the potential difference will decrease, and the electrons will be inducted from the ground back to the silver flakes embedded in the triboelectric skin and generate a negative voltage indicating it is in the opposite direction (Chen et al., 2020 and Lai et al., 2018).

2.5.3 Design of the Sensor

According to (Chen et al., 2019), a sponge-like silicone-based triboelectric nanogenerator (SS-TENG) sensor can be constructed based on triboelectric mechanisms. Such sensor can be integrated into the high compliance SPA to grasp different objects and still to be able to feedback voltage signals. The process of fabricating the SS-TENG sensor is shown in Figure 2.21.

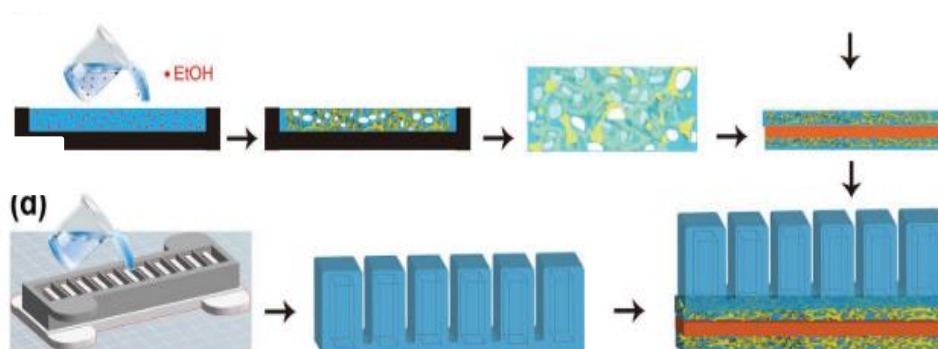


Figure 2.21: Fabrication Process of the SS-TENG sensor (Chen et al., 2019)

A SS-TENG sensor can be constructed based on the fabrication process. The SS-TENG will be integrated into the SPA as a conductive sponge backbone. The pores about 0.5-1 mm diameter on the SS-TENG sensor are distributed randomly. Micro TENG can be formed based on the contact and separation space supplied by the pores. The working principle of the SS-TENG sensor is shown in Figure 2.22.

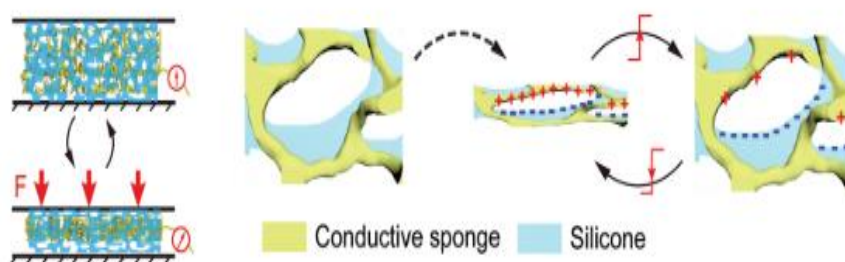


Figure 2.22: Working Principles of SS-TENG sensor (Chen et al., 2019)

The working principle can be explained based on vertical contact-separation mode. When the SS-TENG sensor is pressed, the conductive sponge's surface comes in contact with the silicone's surface. Exchange of charges between conductive sponge and silicone will occur. When the SS-TENG sensor is no longer being pressed, the sponge's nature will cause the gap between the two surfaces to increase. Due to electrostatic induction, it creates a potential difference. The unscreened negative charges on the surface will prompt the flow of electrons from the sponge to the ground. This will induce the accumulation of positive charges in the electrodes and in the end, will generate peak positive voltage. When the SS-TENG sensor is being pressed again, the potential difference will decrease, and the electrons will be inducted from the ground back to the sponge and generating a reversed electric signal (Chen et al., 2020, Chen et al., 2019 and Lai et al., 2018).

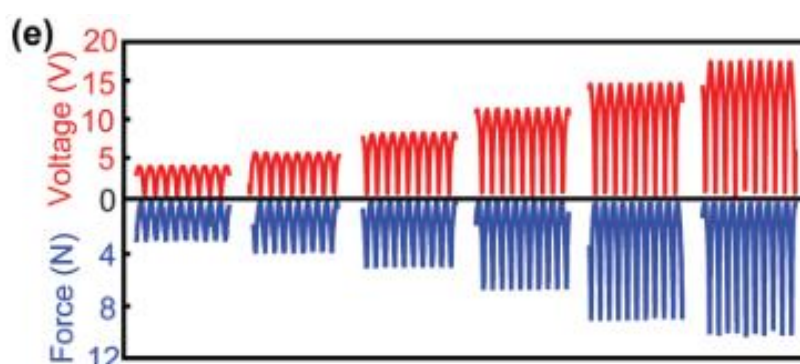


Figure 2.23: Corresponding Open-circuit Voltage under Different Forces (Chen et al., 2019)

Based on Figure 2.23, when the force increased from 3.0 to 9.9 N, the generated open-circuit voltage also increased from 5.5 to 17.1 V. The results show that the generated open-circuit voltage is directly proportional to the force applied. This key finding will be used to determine the effectiveness of the sponge-like TENG sensor in the following chapter.

CHAPTER 3

METHODOLOGY AND WORK PLAN

3.1 Introduction

In this chapter, the procedure to conduct the project will be described thoroughly.

Figure 3.1 shows an overview of the overall project flow.

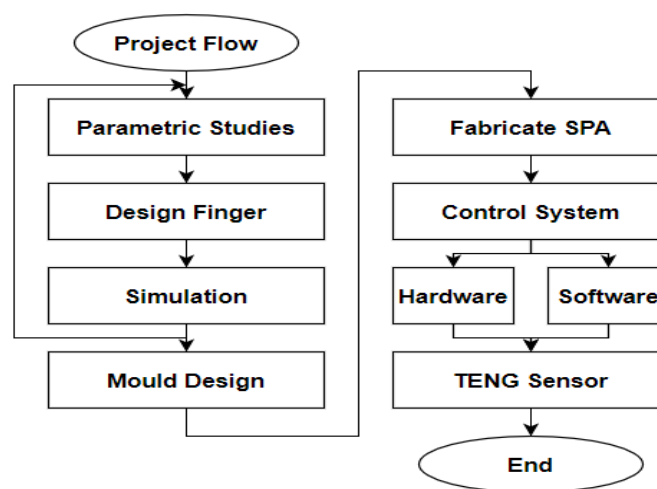


Figure 3.1: Overall Project Flow for an SRG System

Firstly, an in-depth study of how SPA works was conducted to understand how SPA is affected by different parameters. Next, the design of the finger was sketched in SolidWorks. The files were stored in *.step* format, and simulations using Abaqus CAE were performed. The design of the finger has been redesigned until a desirable result is obtained from the simulation. After obtaining a good result, the moulds for the finger were designed and printed using a 3D Printer. The SPAs were fabricated using the 3D printed moulds. The control system, including hardware and software was built once the SPAs are ready to be used. Finally, a TENG sensor was fabricated based on TENG mechanisms. A complete SRG for pick and place applications was produced.

The details of each component will be discussed and explained briefly in the following subchapters.

3.2 Design of SPA using SolidWorks

The design of SPA was the first step in this project, as shown in Figure 2.3.

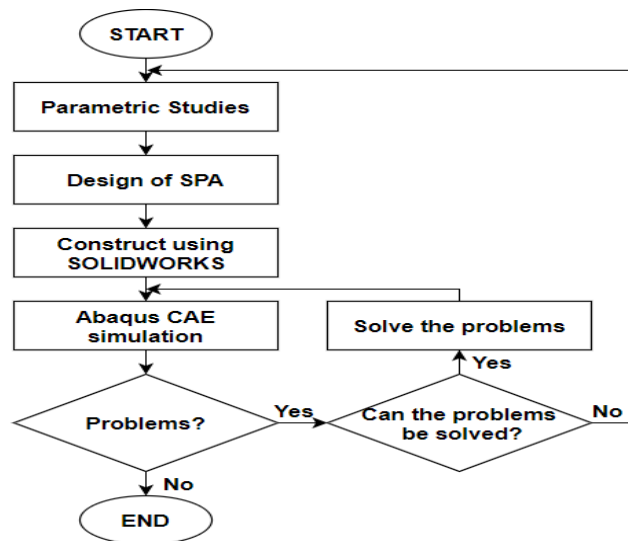


Figure 3.2: Flowchart of Designing the SPA

Each SPA design was simulated using Abaqus CAE to test the feasibility. Each SPA design that failed during the simulation was improved and re-simulated again. Several attempts, such as modifying the shape of the gap, the distance between the gap, the volume of the inner chamber, and the shape of the inner chamber, were performed. Figure 3.3 shows the design of conventional and improved SPA.

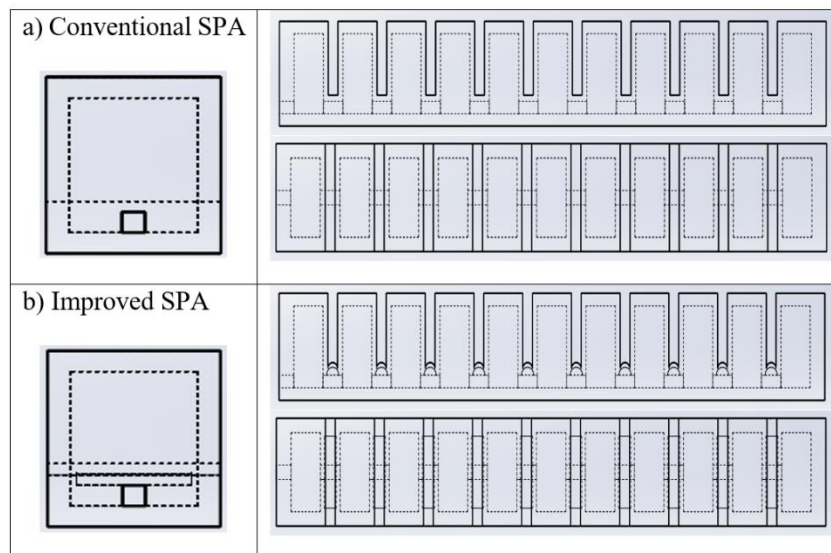


Figure 3.3: (a) Conventional and (b) Improved SPA Sketched in SolidWorks

The dimension of SPA was fixed at width = 1.5 cm, length = 11.2 cm and height = 1.5 + 0.2 cm where 0.2 cm is the base layer. The dimension of the air chamber was fixed at width = 1.1 cm, length = 0.6 cm and height = 1.3 cm. The air chamber channel was fixed at width = 0.2 cm, length = 10.91 cm and height = 0.2 cm. All designed SPAs are attached in Appendix G.

3.3 Abaqus CAE Simulation

As discussed earlier, the designed SPAs will be imported to Abaqus CAE for simulation. Figure 3.4 shows the flowchart to perform the simulation in Abaqus CAE and Figure 3.5 shows the user interface of Abaqus CAE.

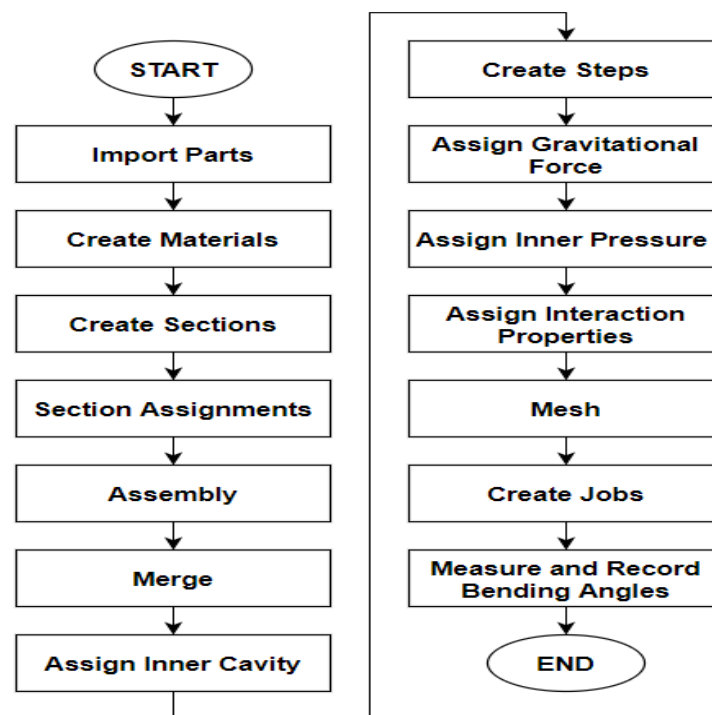


Figure 3.4: Abaqus CAE Simulation Process

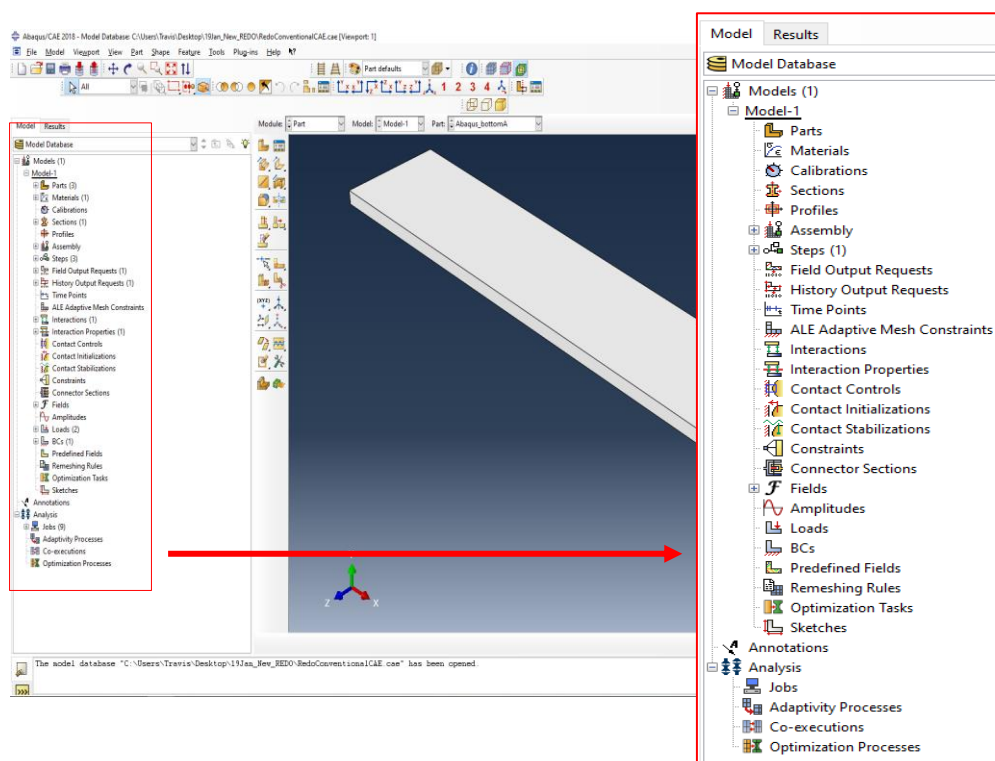


Figure 3.5: User Interface of Abaqus CAE

Firstly, the designed SPA stored in *.step* format was imported to **Parts**. Next, the **Material** was created by assigning *General* → *Density*, *Mass Density* = 1.13 e^{-9} and *Mechanical* → *Elasticity* → *Hyperelastic*, *Strain energy potential* = *Yeoh*, $C10 = 0.11$ and $C20 = 0.02$. A **Section** was created by assigning the created **Material** → *Solid* → *Homogeneous* → *Material 1*. Next, each part's **Section Assignment** was assigned with the created **Section** to assign *Ecoflex* as the material of the part. Once all the parts were assigned with the created **Section**, Upper Layer and Lower Layer was mated using *Create Constraint: Parallel Face* → *Merge* function to merge it in **Assembly**. After merging Upper Layer and Lower Layer, the **Inner Cavity** was created by selecting the chambers' wall inside the SPA. Two **Steps**, including gravitational force and pressure force, were created in **Steps**. Under *Step-Gravitation Force*, *Boundary Condition* was assigned to one of the sidewalls of the SPA. Under *Step-Pressure*, the *magnitude* (pressure) inside the **Inner Cavity** was assigned with a value ranging from 0.005 to 0.04, indicating 5 kPa to 40 kPa. **Interaction Properties** was assigned next. Lastly, the SPA was **Meshed** and allocated with *Global Seeds* = 2.5. The **Element Type** was adjusted to *Hybrid Formulation*. In order to perform the simulation, a **job** was created under **Jobs** and submitted for the simulation. The

jobs were left for running and the status of the *job* will indicate “completed” after 30 minutes to 45 minutes. The bending angle of the SPA was obtained by right-clicking *job* → *results* → *Tools* → *Query* → *Angle* → *3 Nodes* and 3 nodes were selected, as shown in Figure 3.6. The bending angle was recorded in Microsoft Excel for further analysis.

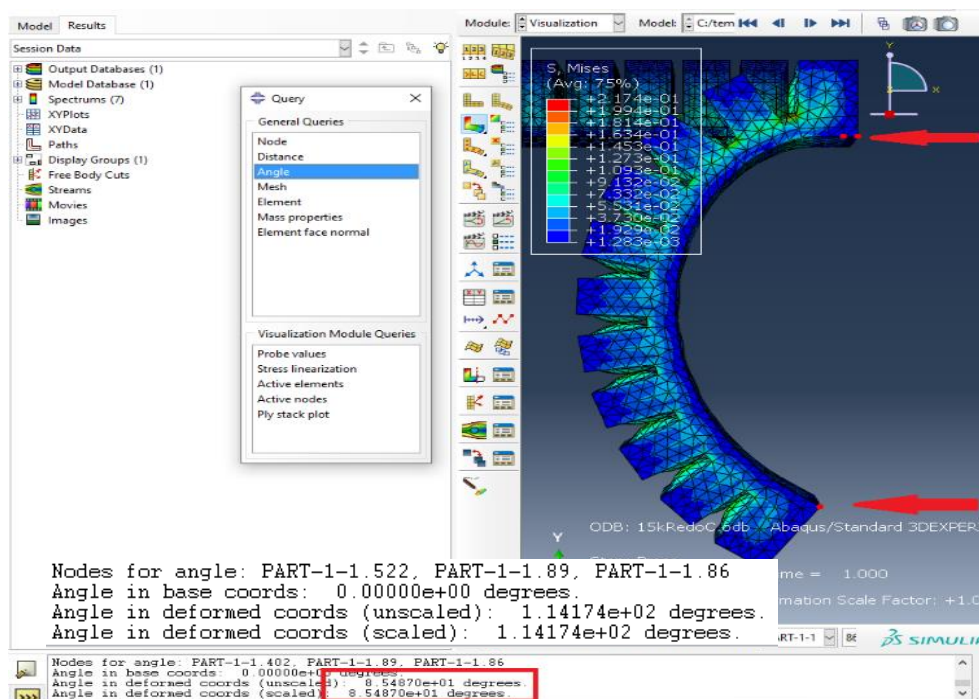


Figure 3.6: Simulated Bending Angle Measured using 3 Nodes in Abaqus CAE

3.4 SRG Fabrication Process

Once the SPA design was finalized, the moulds and the finger holder for the SPA were designed in SolidWorks. The fabrication process was started once the designed moulds and finger holder were printed using a 3D printer.

3.4.1 Mould and SPA Holder Design

The moulds were designed based on the conventional and improved SPA, and the process of designing the mould is shown in Figure 3.7.

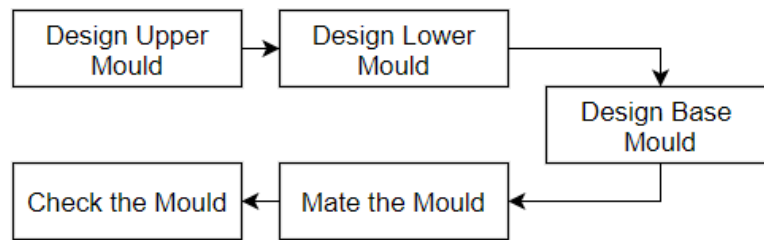


Figure 3.7: Block Diagram for Mould Design

Firstly, Upper Mould and Lower Mould were sketched in SolidWorks and followed by the Base Mould. Upper Mould and Lower Mould were mated together to ensure the moulds were properly designed. Figure 3.8 shows the moulds design in SolidWorks. Figure 3.9 shows the 3D printed moulds, and Figure 3.10 shows the SPA holder to hold the fabricated SPA.

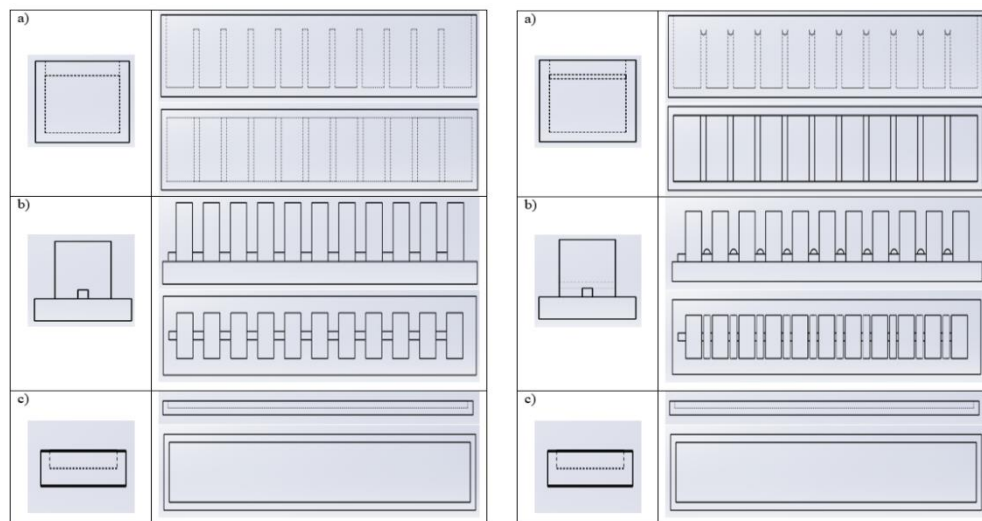


Figure 3.8: Conventional SPA Moulds (left) and Improved SPA Moulds (Right)



Figure 3.9: 3D Printed Moulds for Conventional (left) and Improved (right) SPA

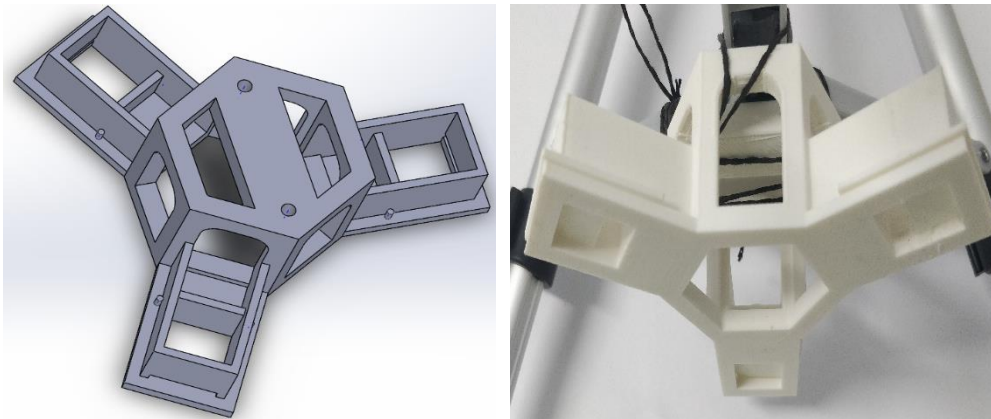


Figure 3.10: SPA Holder Sketch (left) and 3D Printed SPA Holder (right)

3.4.2 Fabrication of SPA

The fabrication process of the SPA can be summarised into a flowchart, as shown in Figure 3.11.

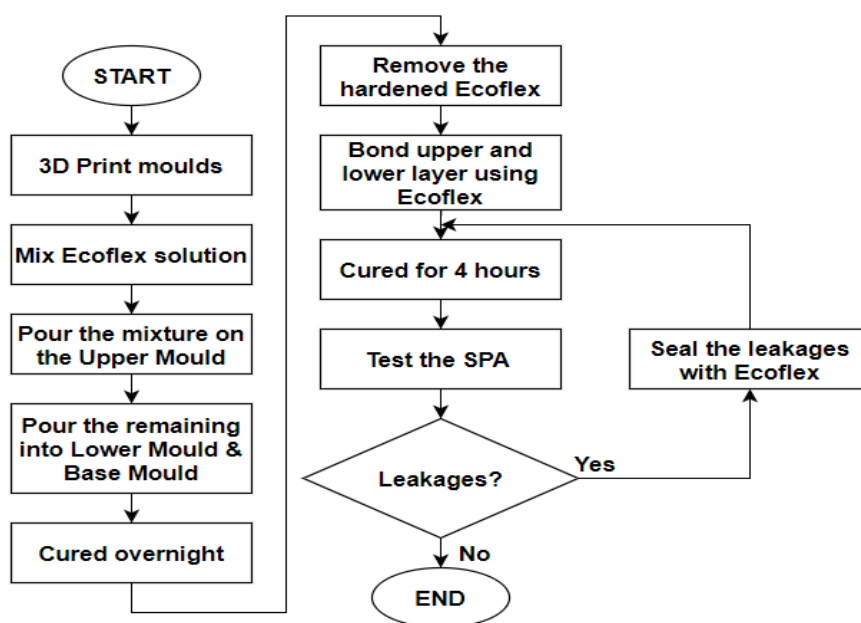


Figure 3.11: SPA Fabrication Process

Ecoflex Solution A and B were mixed based on 1:1 ratio using a precise electronic balance. The mixture was poured on the Upper Mould to prevent the formation of air bubbles. Next, the mixture was poured into the Lower Mould and Base Mould. The Upper Mould was mated with the Lower Mould. The excess Ecoflex mixture was removed using a disposable plastic spoon and the

mixture was left to cure overnight. The hardened Ecoflex was removed from the mould with the aid of an Isopropyl Alcohol. The upper layer was bonded together with the lower layer by applying a thin layer of Ecoflex. The fabricated SPAs were tested for any leakages after being cured for 4 hours. Any found leakages were sealed with Ecoflex. Figure 3.12 shows the upper layer, lower layer, and fabricated SPA.

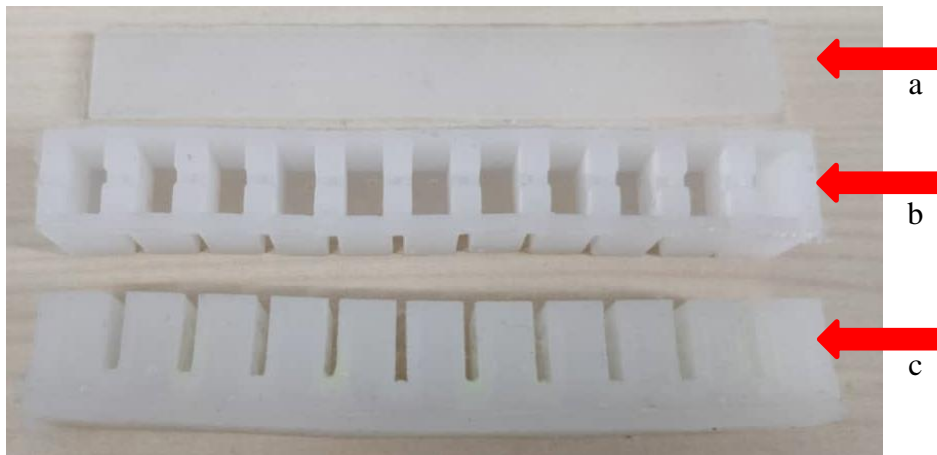


Figure 3.12: (a) Lower Layer, (b) Upper Layer, and (c) Fabricated SPA

3.4.3 Soft Robotic Gripper, SRG

The SRG was built using three SPAs and a 3D printed SPA holder, as shown in Figure 3.13.

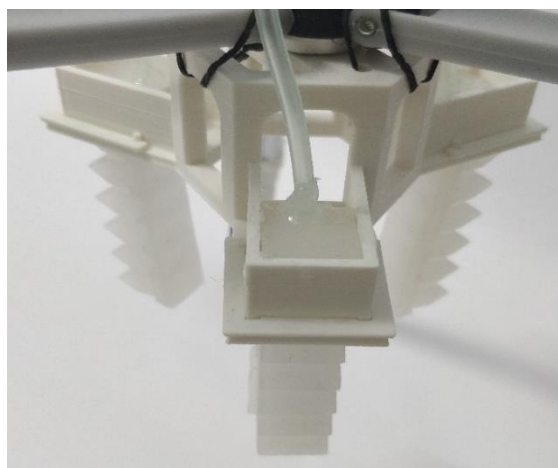


Figure 3.13: An SRG with 3 SPAs connected to Oxygen Nasal Cannula

An Oxygen Nasal Cannula was used to supply pneumatic pressure to the SPAs for inflation and deflation. The tube connecting to the SPA was sealed with Clear RTV Silicone to prevent any leakages as it offered excellent adhesion, elasticity and ability to withstand 5000 psi pressure which is about 34473.79 kPa. The SRG was cured overnight and tested using a syringe connecting to the tube. SRG was submerged in water during the last stage of quality checking to observe any formation of air bubbles. In the case whereby air bubbles were absent, the fabrication of SRG was claimed to be completed.

3.5 Control System

The control system to inflate and deflate the SRG was constructed after the SRG was successfully built. The control system of this project was separated into hardware and software to achieve the user requirements. The user requirements, functional requirements, system and equipment requirements, and system specifications stated below.

User Requirements

Module 1:

When the “ExtendButton” button is pressed, the linear actuator will retract to deflate the finger, pause, then only extend to inflate the finger via the 200 ml syringe.

Module 2:

When the “RetractButton” button is pressed, the linear actuator will retract to deflate the finger via the 200 ml syringe.

Module 3 (Separated Code):

When pressure is supplied, the *serial monitor* will show the current pressure read by the pressure sensor.

Functional Requirements

Module 1:

When the ExtendButton is pressed, ExtendButton is equal to 0 (Pullup resistor, the state is always 1, when pressed is 0). ESP32 will send signal a to L298N to drive the linear actuator to retract → pause → extend based on *delay()*. OLED will display “Status: Retract → Delay → Extend”.

Module 2:

When the RetractButton is pressed, RetractButton is equal to 0 (Pullup resistor, the state is always 1, when pressed is 0). ESP32 will send a signal to L298N to drive the linear actuator to retract for a period based on *delay()*. OLED will display “Status: Retract”.

Module 3 (Separated Code):

Enable ADC, read every 1s. Convert 0-4095 ADC value into 0-3.3 V. Convert the voltage value to 5V. Apply the formula from the MPX5500DP datasheet and display the pressure value in kPa via *Serial.print()*.

Table 3.1 shows the system and equipment requirements, and Table 3.2 shows the system specifications. Figure 3.14 shows the hardware circuit.

Table 3.1: System and Equipment Requirements

1) ESP32	2) 12 V, 2 A Linear Actuator
3) 10 and 1 k Ω resistor	4) L298N Motor Driver
5) 2 Pushbuttons	6) OLED
7) 12 V, 2 A Power Adapter	8) MPX5500DP Pressure Sensor

Table 3.2: System Specifications

Input	Output
ExtendButton	MotorPin1
RetractButton	MotorPin2
Sensor	OLED

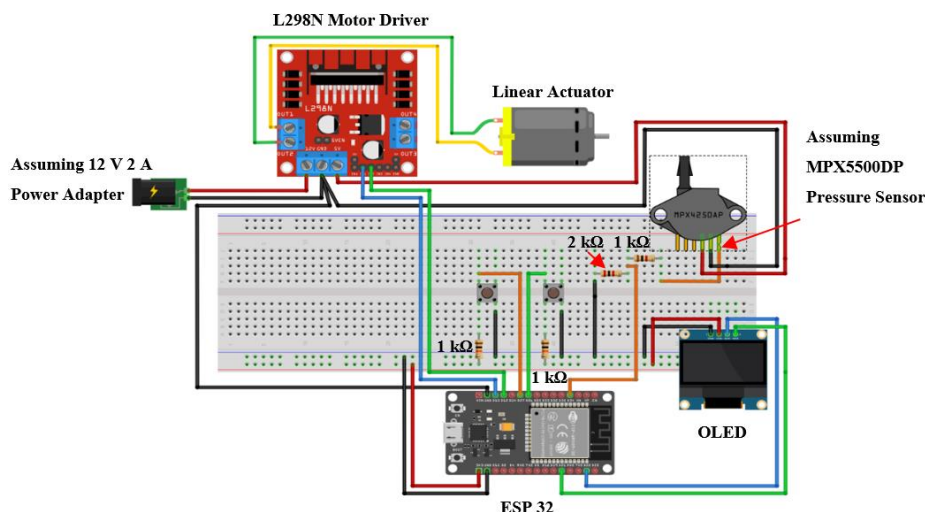


Figure 3.14: Hardware Circuit

GPIO12 and GPIO13 were connected to L298N IN1 and IN2, respectively. A 12 V 2 A power adapter was used to power up the L298N. The linear actuator was connected to L298N Motor1 OUT1 and OUT2. The ground of L298N and ESP32 were connected to share the same ground. The pressure sensor was powered up by the 5 V supplying from L298N. The output voltage of MPX5500DP was connected to a voltage divider to lower the voltage from 0 – 5 V to 0 to 3.3 V as ESP32 maximum input voltage is 3.3 V. The converted voltage was connected to GPIO34. The OLED was powered up by the 3.3 V supplying from ESP32, and the SCL and SDA were connected to GPIO22 and GPIO21, respectively.

Once the circuit was built, the algorithms were written in Arduino IDE using C programming language based on Figure 3.15 and Figure 3.16. The pressure values obtained from MPX5500DP were recorded as attached in Appendix H. Figure 3.17 shows the hardware prototype to control the SRG.

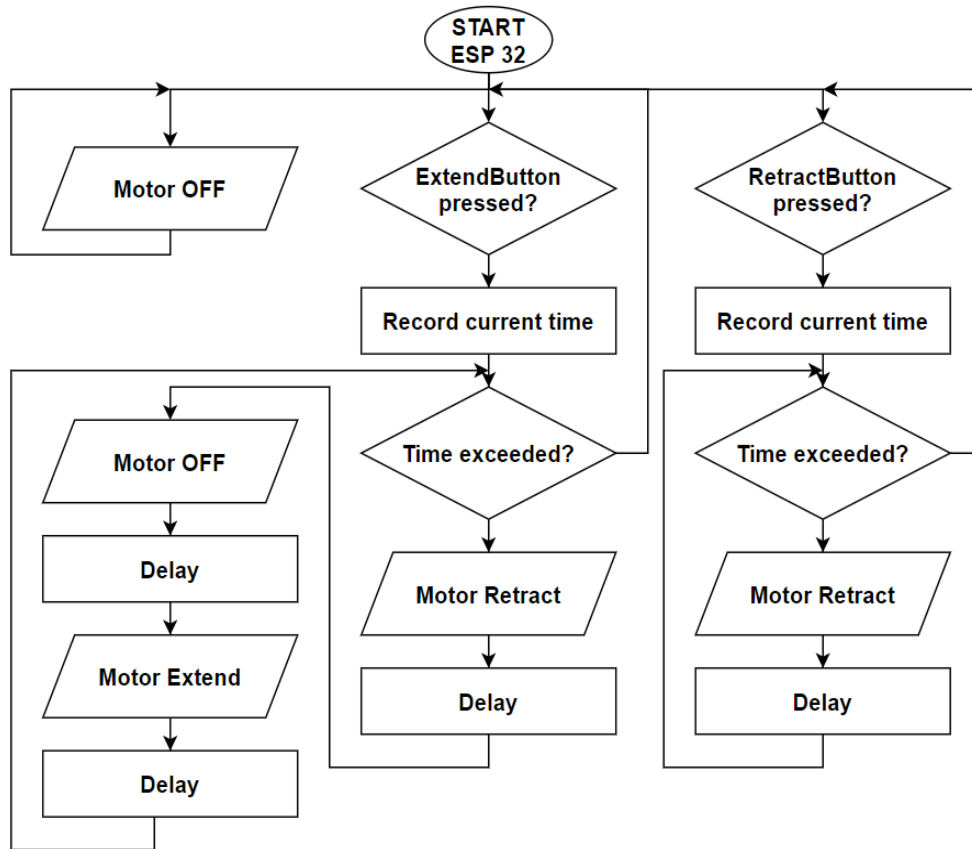


Figure 3.15: Overall Flowchart of the System

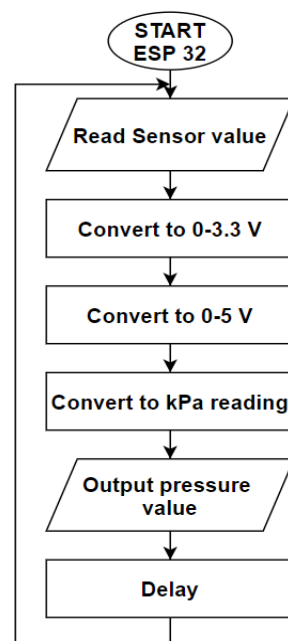


Figure 3.16: Flowchart of the Pressure Sensor

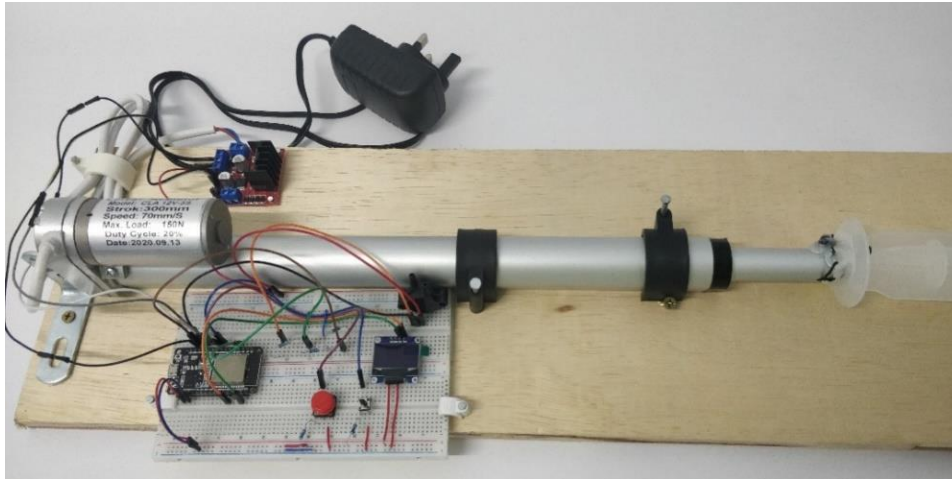


Figure 3.17: Hardware Prototype Attached with a 200 ml Syringe

3.6 Fabrication of TENG Sensor

The process of fabricating the TENG sensor is as shown in Figure 3.18.

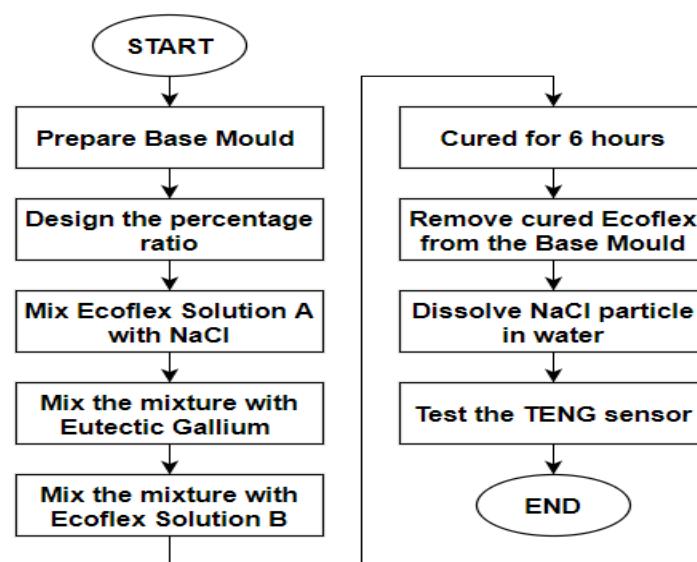


Figure 3.18: Fabrication of Sponge-like TENG Sensor.

The percentage ratio was designed such that 22% of Ecoflex, 13% of Eutectic Gallium and 65% of Sodium Chloride, NaCl. First of all, 11% of Ecoflex Solution A was mixed with 65% of NaCl followed by 13% of Eutectic Gallium. The mixture was stirred for 10 minutes to ensure even mixing. Next, 11% of Ecoflex Solution B was added into the mixture and stirred for 5 minutes. The mixture was cured for 6 hours, and the cured prototype was removed from the base mould. The prototype was immersed in water with a temperature of

60 °C with a magnetic stirrer to dissolve NaCl particles to create the porous structures. The prototype was ready to be used once the NaCl particles were fully dissolved.

The fabricated sensor was attached to the SPA, as shown in Figure 3.19. A copper cable connecting to a multimeter was placed between the TENG sensor and the SPA.

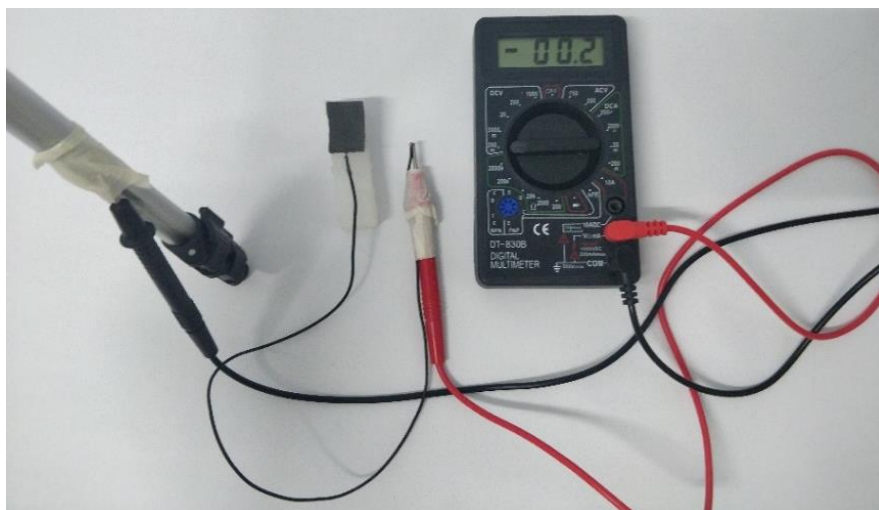


Figure 3.19: SPA Attached with a Sponge-like TENG Sensor

CHAPTER 4

RESULTS AND DISCUSSION

4.1 Introduction

In this chapter, the simulation and experimental results will first be discussed. Several parametric studies that would affect the bending angle of the SPA were conducted using Abaqus CAE. The simulated bending angles were recorded in tables and will be presenting using graphs. The SPA was improved based on the simulated results and eventually, producing the final design of the SPA. The steps of producing the improved SPA design will be discussed extensively by using visual illustrations, such as graphs and diagrams. The differences between the simulation and experimental results are compared using line graphs followed by explaining the hardware prototype features. Lastly, the constructed sponge-like TENG sensor will be reviewed.

4.2 Simulation and Experimental Results

In order to characterize the SPA, several approaches were taken, such as studying the gap distance between the SPA, the volume of the air chambers, the shape of the gap as well as the design of the air chambers. Each study is interrelated with each other in contributing to the final design of the SPA. Therefore, the outcomes of the studies will be discussed in the following subchapters.

4.2.1 Study on SPA Gap Distance

The study on SPA gap distance was conducted first. The purpose is to prove the gap distance between the SPA chamber will only affect the shape of the inflated SPA instead of the bending angle. As shown in Figure 4.1, the gap between SPA chambers was increased from 2 mm to 8 mm.

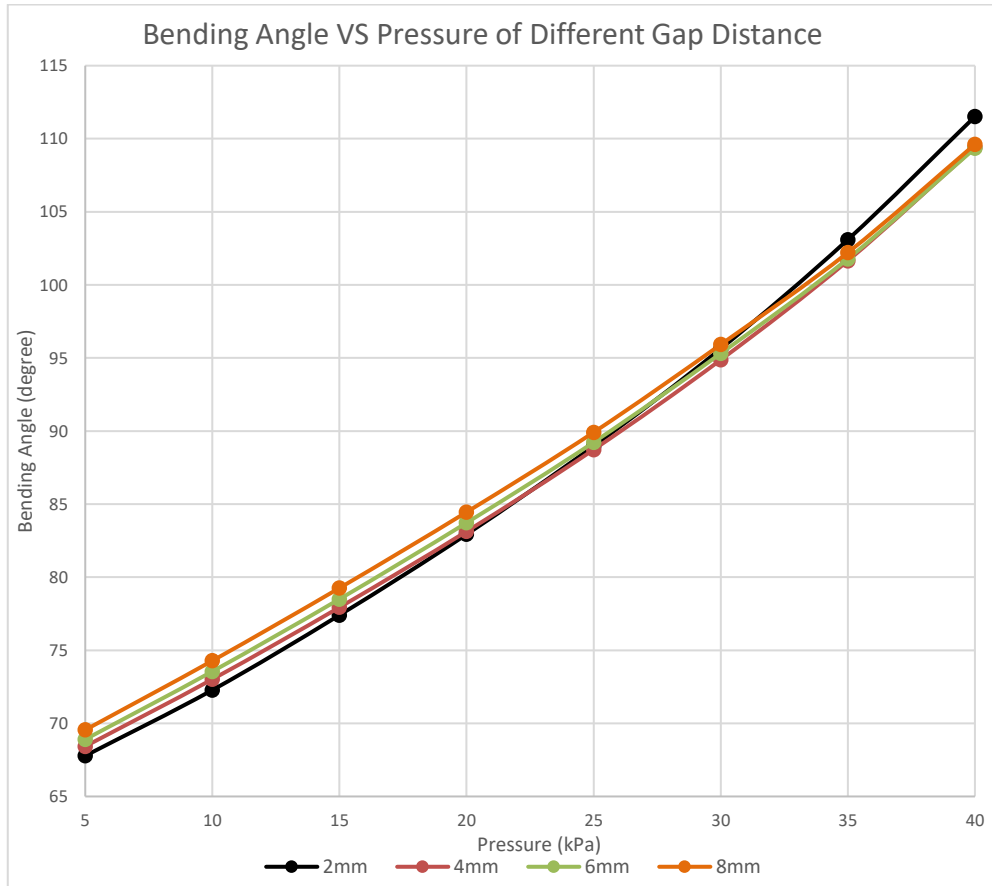


Figure 4.1: Bending Angle of Different Gap Distance

The simulated bending angles are relatively closed to each other. For a pressure of 40 kPa, the percentage difference of a gap distance for 2 mm and 8 mm was 1.7% different. It is relatively small considering such a big gap difference. However, the shape of the actuated SPA has an obvious difference, as shown in Figure 4.2, where the green arrow is pointing to the SPA with a 2 mm gap while the red arrow is pointing to the SPA with an 8 mm gap.

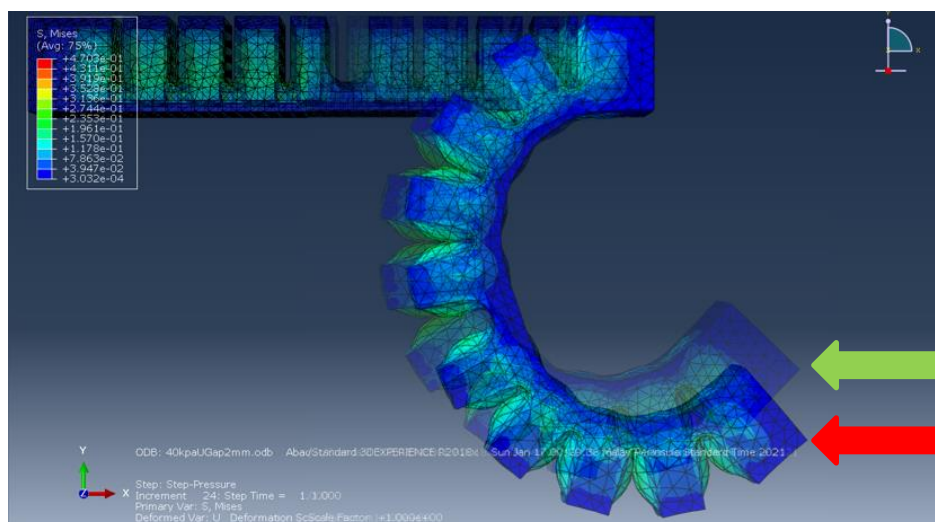


Figure 4.2: Comparison between 2 mm (green) and 8 mm (red) Gap Distance

Although the simulated bending angles are relatively closed, 111.52° for 2 mm gap and 109.41° for 8 mm gap; the bending shape for the 8 mm gap has a straighter form, while the 2 mm gap has a curvature shape. This allowed flexibility in designing the finger based on the grabbed object.

4.2.2 Study on SPA Air Chamber Volume

Next, the effect of SPA air chamber volume was studied. The purpose is to observe whether the overall bending angle of the SPA is affected by the volume of the air chambers. The air chambers' height was altered from 1.3 cm to 0.9 cm resulted in the total volume reduced from 9.438 cm^3 to 6.453 cm^3 . The simulated bending angles are presented in the bar chart, as shown in Figure 4.3.

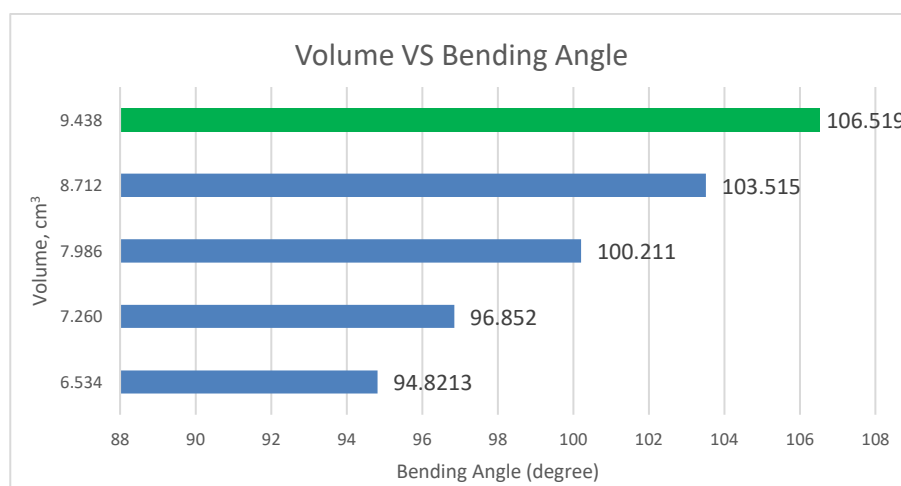


Figure 4.3: Bending Angle of Different Air Chamber Volume

The study's key finding is the volume of the air chamber played an important role in producing high bending angles. As shown in Figure 4.3, the bending angle is directly proportional to the volume of the air chamber. This study will contribute to designing the final improved SPA.

4.2.3 Study on SPA Gap Shape

Furthermore, consideration of SPA gap shape was taken such that several designs of gap shape were simulated. Figure 4.4 shows the design of the gap shape. The simulated bending angles were recorded to generate line graphs, as shown in Figure 4.5 and Figure 4.6.

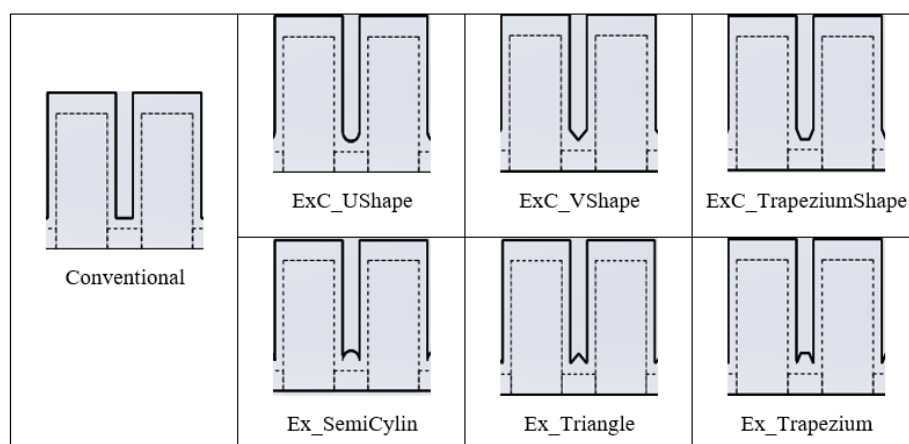


Figure 4.4: Design of SPA Gap Shape

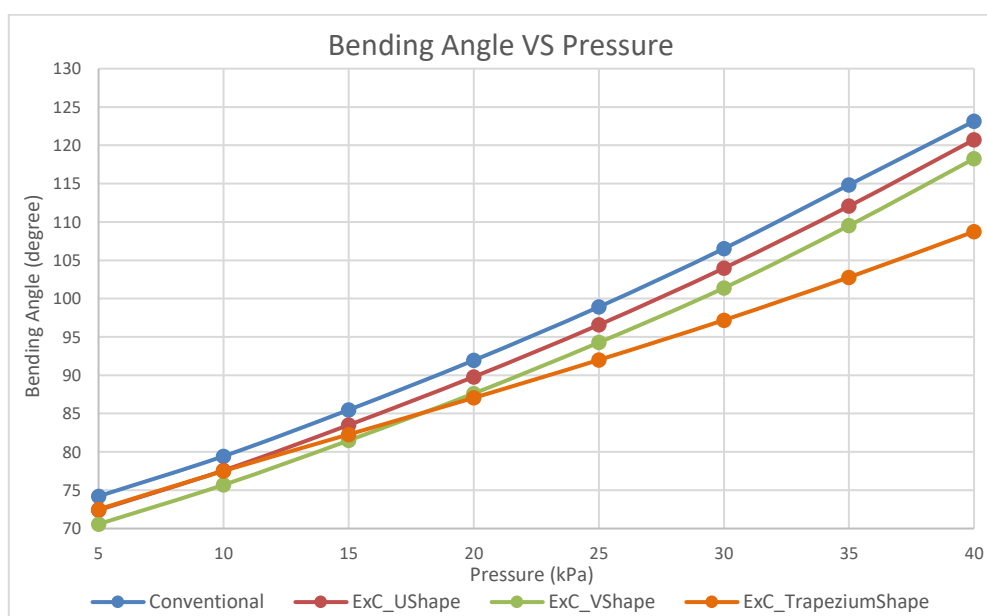


Figure 4.5: Bending Angle of Different Gap Shape (Extruded Cut)

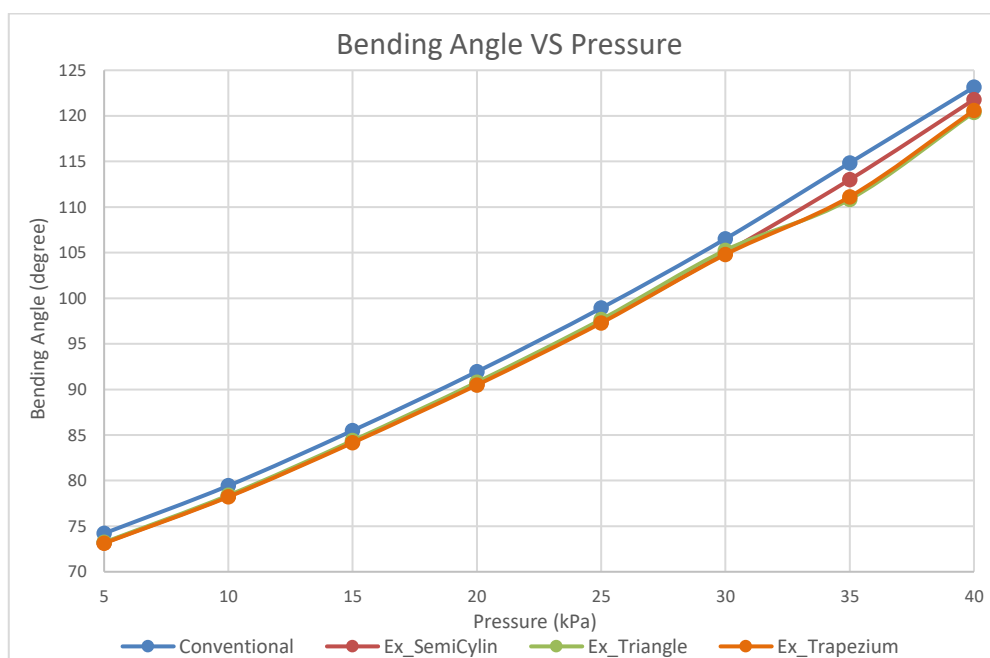


Figure 4.6: Bending Angle of Different Gap Shape (Extruded)

Comparing Figure 4.5 and Figure 4.6, the simulated bending angles in Figure 4.6 are closer to the conventional design. Based on the studies, it can be concluded that the extruded designs have higher bending angles compared to the extruded cut designs. With this information, the extruded designs can be further improved by considering other factors that would affect the overall bending angles. Since Ex_SemiCylin has the bending angles closest to the conventional design with only a 1.1% percentage difference. As a result, Ex_SemiCylin was chosen to be further improved.

4.2.4 Improved SPA

Based on the key finding in Chapter 4.2.2, the higher the air chamber volume, the higher the bending angle of the SPA. The Ex_SemiCylin was improved by adding semi-cylindrical air chamber in the SPA, as shown in Figure 4.7. The simulated bending angles of each different air chamber diameter were recorded to produce a line graph, as displayed in Figure 4.8.

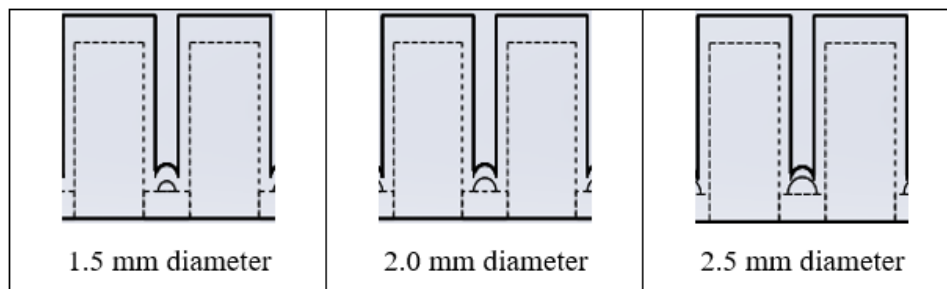


Figure 4.7: Additional Semi-cylindrical Air Chamber

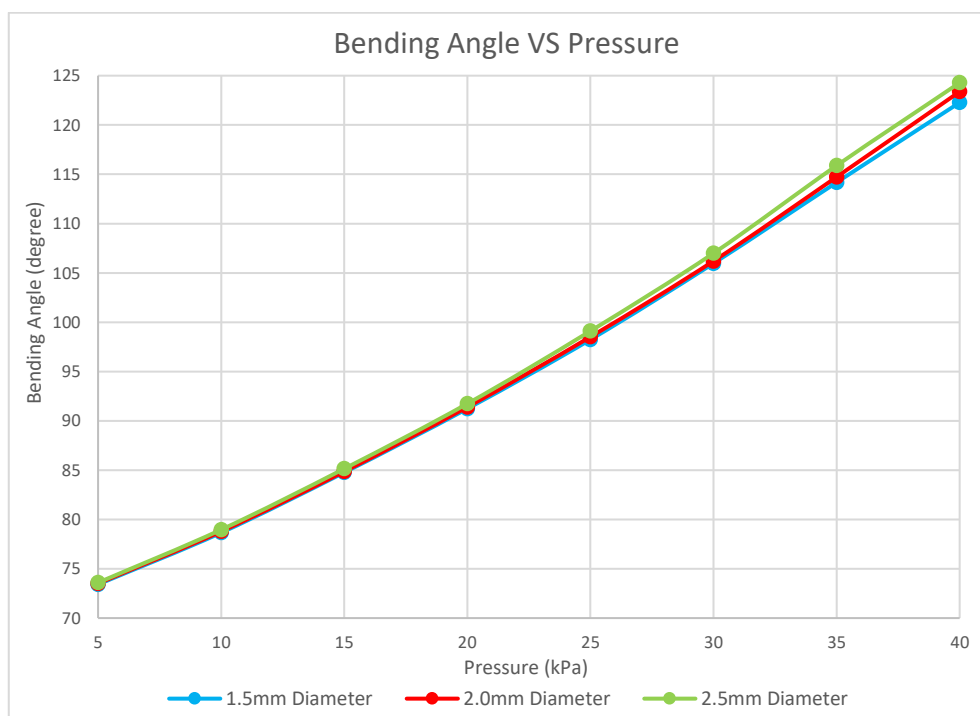


Figure 4.8: Bending Angle of Different Diameter of the Semi-cylindrical Air Chamber

The SPA with 2.5 mm diameter semi-cylindrical air chamber stands out from other parameters with 124.282° , which is 0.73% and 1.64% better than the 2.0 mm diameter and the 1.5 mm diameter, respectively. This allowed the Ex_SemiCylin with an additional 2.5 mm diameter semi-cylindrical air chamber to be the improved SPA. A clear comparison between the conventional SPA and improved SPA is shown in Figure 4.9 and Figure 4.10.

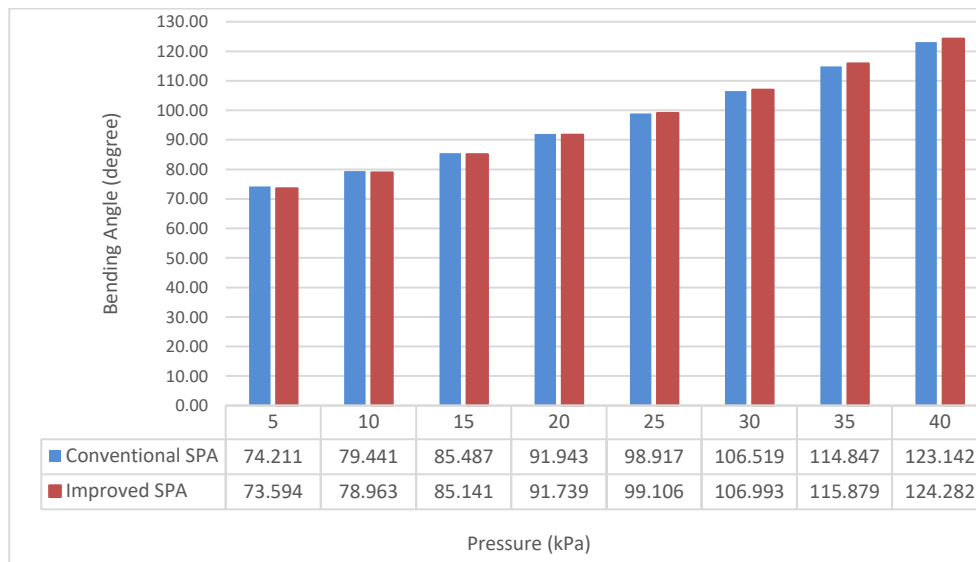


Figure 4.9: Comparison between Conventional SPA and Improved SPA

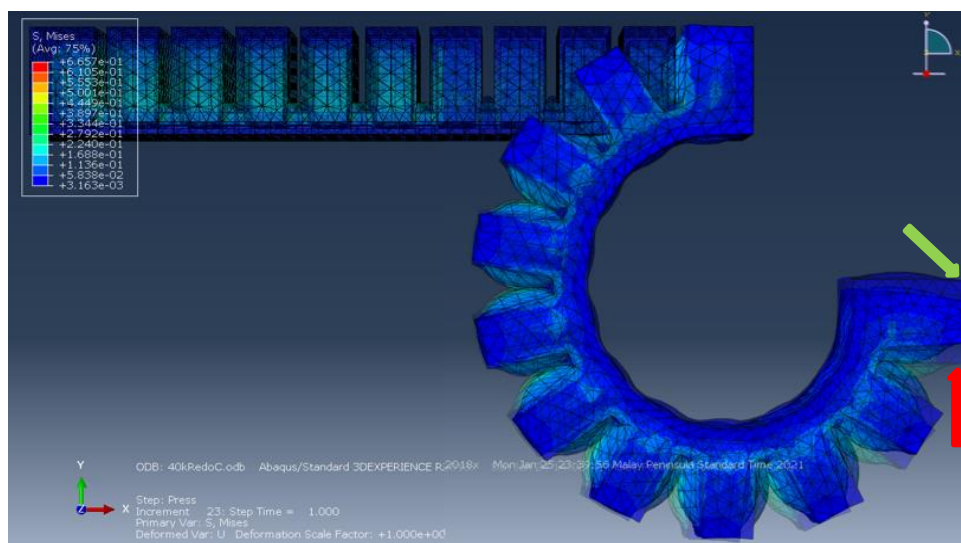


Figure 4.10: Comparison between Conventional SPA (red) and Improved SPA (green)

Based on the figures, it can be noticed that the performance of the improved SPA has higher bending angles as compare to conventional SPA. The improved SPA was approximately 0.9258% better than the conventional SPA at 40 kPa. From 5 kPa to 20 kPa, the simulated bending angles of the improved SPA are lower than the conventional SPA. A possible reason is that the volume in the improved SPA is larger than the conventional SPA. Hence, it required more pressure to actuate. However, from 25 kPa to 40 kPa, the simulated bending angles are significantly higher than the conventional SPA. This

phenomenon could be due to the design's nature, allowing it to actuate more than the conventional design. The findings of this study offered a unique characteristic to the improved SPA.

Finally, the simulation results were compared with experimental results. The comparison between simulation and experimental results is shown in Figure 4.11. The experimental results were recorded by measuring the bending angle on graph papers manually. Each experiment was repeated five times to obtain average bending angle.

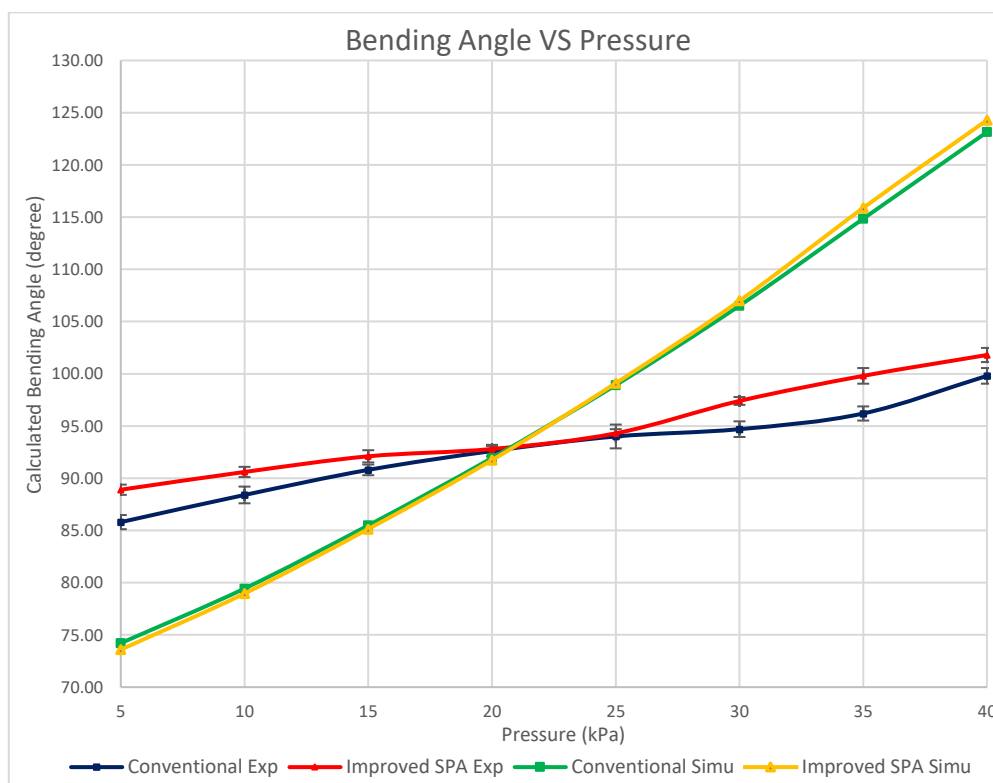


Figure 4.11: Simulation Results and Experimental Results

By looking at the experimental results, the bending angles of the improved SPA are significantly larger than the conventional SPA. This shows the improved SPA has a higher performance than the conventional SPA experimentally. Besides, the improved SPA's bending angles for both simulation and experimental have increased significantly from 25 kPa to 40 kPa, as shown in Figure 4.11. However, the comparison between simulation and experiment is not ideal. Figure 4.12 shows the comparison between the simulation results and experimental results of the improved SPA.

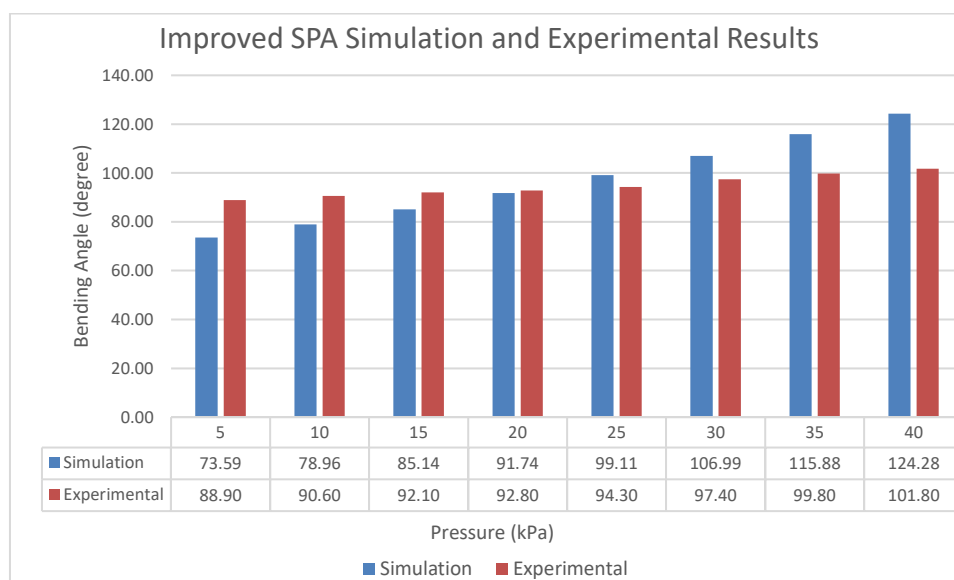


Figure 4.12: Comparison between Simulation Results and Experimental Results of Improved SPA

The experimental results have significantly lower bending angles compared to the simulation results with a percentage difference of 22.8% at 40 kPa. The major difference between the simulation results and experimental results could be due to leaking of pneumatic pressure or from equipment fatigue. Besides, the Abaqus CAE simulation software considered the perfect condition. Externalities, such as changes in the ambient environment as well as differences in material quality might not be taken into account during the experiment. Therefore, a slight deviation between simulation and experimental results are unavoidable. That being said, the experimental results still prove the theory that bending angles are directly proportional to the pressure supplied. This is because the experimental results of improved SPA increased from 88.90° to 101.80° as the pressure supplied increased from 5 kPa to 40 kPa. The findings of this study proved the improved SPA is better than the conventional SPA.

4.3 Hardware Features

The constructed SRG was able to grab an object by inflating and deflating the SPA. This can be achieved by the control system prototype, as shown in Chapter 3.5. Figure 4.13 shows the SRG in its deflated and inflated status.

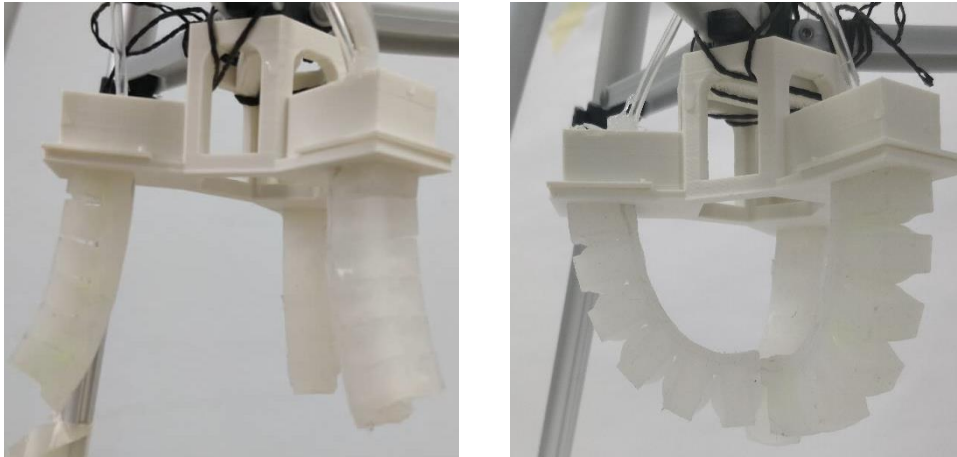


Figure 4.13: Deflated (left) and Inflated (right)

The SRG was designed to first deflate in order to increase the grabbing surface area. By doing so, it can grab objects larger than the SPA holder. Next, the system will have a short delay of 1 second before actuating the SRG. The supplied pneumatic pressure will cause the SPA to inflate and grab the object. Figure 4.14 shows the SRG grabbing objects, such as an aluminium can, a sphere, a rectangle box, and a cylindrical bottle.

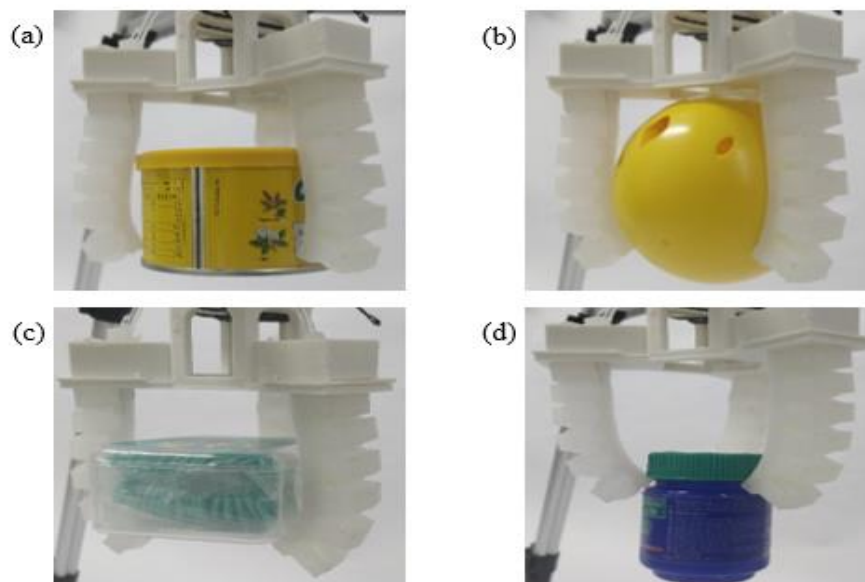


Figure 4.14: SRG Grabbing Different Objects (a)Aluminium Can, (b)Sphere, (c)Rectangle Box, and (d)Cylindrical Bottle

The improved SPA with a dimension of 1.5 cm x 7.3 cm x 1.7 cm, 7 chambers supplied with 40 ml pneumatic pressure was able to grab objects with weight of 40.03 g (aluminium can), 54.46 g (sphere), 52.20 g (rectangle box) and 21.96 g (cylinder bottle). Furthermore, the OLED display on the control system prototype was used to observe the status of the linear actuator, such as “Retract”, “Delay”, “Extend”, and “Off”, as shown in Figure 4.15.

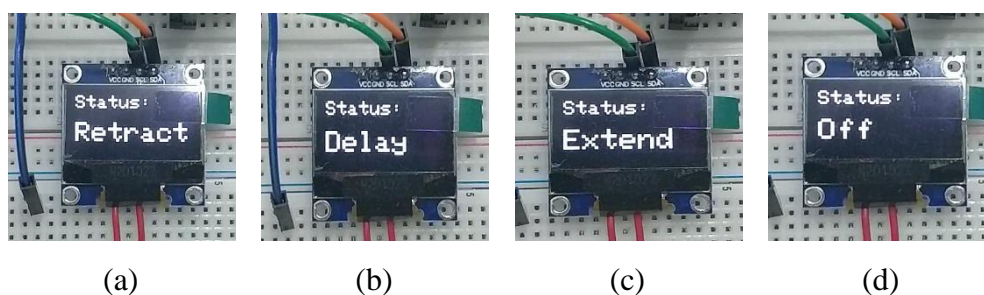


Figure 4.15: OLED Status

4.4 TENG Sensor

The peak voltages produce by the TENG sensor due to contact electrification, and electrostatic induction were recorded and presented in Figure 4.16. Different materials, such as finger, aluminium and plastic were used as a functional layer.

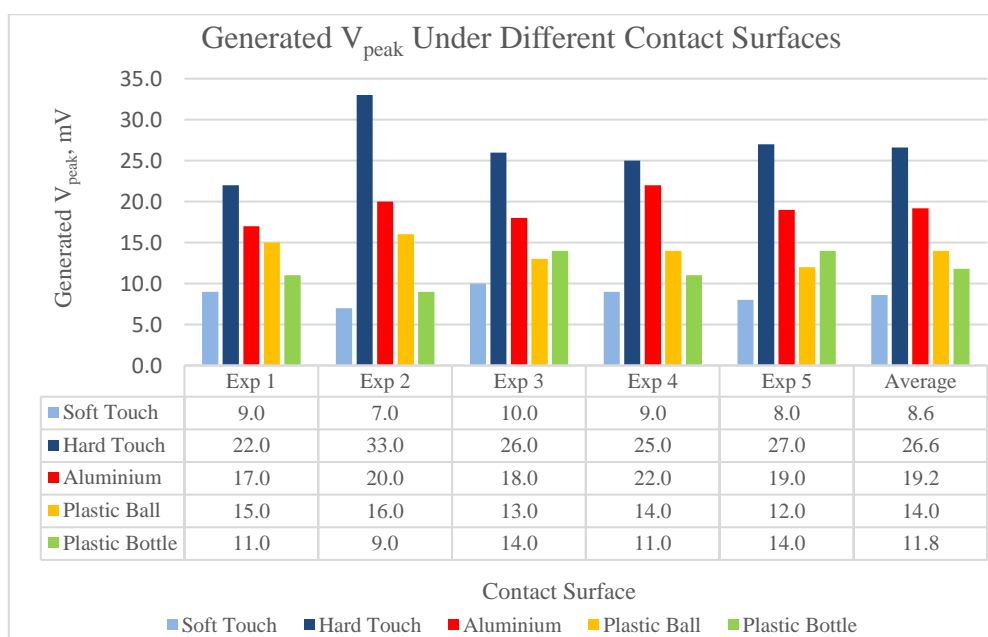


Figure 4.16: Generated V_{peak} by Sponge-like TENG Sensor

Referring to the average peak voltage generated by the soft touch and hard touch whereby soft touch was a low-pressure finger touch, and hard touch is otherwise. It has provided a shred of clear evidence that proves the results obtained from Chen et al., (2019), as shown in Figure 2.23. The authors proposed the output voltage is directly proportional to the force applied. The average result of hard touch has a significantly larger generated peak voltage, with it being approximately 209.3% higher than soft touch.

Besides, the voltages generated by hard touch were also the highest. Among the materials chosen, human skin showed the greatest output peak voltage due to it is more tribo-positive than aluminium and plastic materials, which has a greater tendency to donate electrons to other objects. This led to another key finding where studies proposed when a material towards the bottom of the series (most triboelectrically negative) came in contact with material towards the top of the series (most triboelectrically positive), the charge transferred will be greater, and therefore, generate a higher peak voltage (Wang et al., 2016). Since human skin is more triboelectrically positive than aluminium based on the triboelectric series as attached in Appendix I. Therefore, the voltage generated from human touch should be greater than aluminium material. The results proved the theory as the aluminium peak voltage generated is 19.2 mV, 38.54% lower than peak voltage generated by hard touch.

The results generated by the fabricated sponge-like TENG are ideal, and this useful information produced by the sensor can be utilized to build an object recognition system. Different materials and shapes will produce a unique peak voltage, and the generated voltage can be used to identify the object.

CHAPTER 5

CONCLUSIONS AND RECOMMENDATIONS

5.1 Conclusions

This project has given a unique character to the SRG. The aims of this project have been successfully achieved. Several studies about the working principle of an SRG based on previous SPA designs and factors that affect the performance of the SPA were conducted. An improved SPA design with an extruded semi cylinder between the SPA gap and additional 2.5 mm semi-cylindrical air chamber was proposed. The improved SPA was proven with a 0.9258% bending angle higher than the conventional SPA based on the obtained simulation results. The simulation results were compared with the experimental results. In addition, the percentage error between the simulation and experimental results were identified.

Besides, this project has also introduced a sponge-like soft sensor based on single-electrode mode. It was found that the generated peak voltages are in agreement with previous works. The results obtained are significant as it supports the statements made by researchers about TENG.

In short, this project has proven to be successful as it managed to characterize the SRG with an improved SPA design, can perform pick and place applications and is introduced to a soft sensor based on new technology, TENG.

5.2 Recommendations for Future Work

Several improvements can be made to this experiment, including but not limited to using a piece of more precise equipment, such as an electronic pressure regulator to measure the actual pressure supplied to the SPA. Doing so can reduce the percentage error between simulation and experimental results to an acceptable range.

Besides, the information obtained from the sponge-like TENG sensor can be harvested and fed into the microcontroller as a feedback system. The proposed suggestion will be able to improve the overall performance of the SRG.

The information obtained can also be used to build a real-time object recognition system and enhance the system via machine learning features.

REFERENCES

- Adam Bilodeau, R., White, E.L. and Kramer, R.K., 2015. Monolithic fabrication of sensors and actuators in a soft robotic gripper. *IEEE International Conference on Intelligent Robots and Systems*, 2015-Decem, pp.2324–2329.
- Badamasi, Y.A., 2014. The working principle of an Arduino. *Proceedings of the 11th International Conference on Electronics, Computer and Computation, ICECCO 2014*.
- Chen, J., Chen, B., Han, K., Tang, W. and Wang, Z.L., 2019. A Triboelectric Nanogenerator as a Self-Powered Sensor for a Soft–Rigid Hybrid Actuator. *Advanced Materials Technologies*, 4(9), pp.1–7.
- Chen, S., Pang, Y., Yuan, H., Tan, X. and Cao, C., 2020. Smart Soft Actuators and Grippers Enabled by Self-Powered Tribo-Skins. *Advanced Materials Technologies*, 5(4), pp.1–10.
- Diaz, A.F. and Felix-Navarro, R.M., 2004. A semi-quantitative tribo-electric series for polymeric materials: The influence of chemical structure and properties. *Journal of Electrostatics*, 62(4), pp.277–290.
- Ge, L., Dong, L., Wang, D., Ge, Q. and Gu, G., 2018. A digital light processing 3D printer for fast and high-precision fabrication of soft pneumatic actuators. *Sensors and Actuators, A: Physical*, 273, pp.285–292.
- Hao, Y., Gong, Z., Xie, Z., Guan, S., Yang, X., Ren, Z., Wang, T. and Wen, L., 2016. Universal soft pneumatic robotic gripper with variable effective length. In: *Chinese Control Conference, CCC. TCCT*. pp.6109–6114.
- Haque, R.I., Chandran, O., Lani, S. and Briand, D., 2018. Nano Energy Self-powered triboelectric touch sensor made of 3D printed materials. *Nano Energy*, [online] 52(July), pp.54–62. Available at: <<https://doi.org/10.1016/j.nanoen.2018.07.038>>.
- Herianto, Irawan, W., Ritonga, A.S. and Prastowo, A., 2019. Design and

fabrication in the loop of soft pneumatic actuators using fused deposition modelling. *Sensors and Actuators, A: Physical*, [online] 298, p.111556. Available at: <<https://doi.org/10.1016/j.sna.2019.111556>>.

Ilievski, F., Mazzeo, A.D., Shepherd, R.F., Chen, X. and Whitesides, G.M., 2011. Soft robotics for chemists. *Angewandte Chemie - International Edition*, 50(8), pp.1890–1895.

Kim, D.W., Lee, J.H., Kim, J.K. and Jeong, U., 2020. Material aspects of triboelectric energy generation and sensors. *NPG Asia Materials*, [online] 12(1). Available at: <<http://dx.doi.org/10.1038/s41427-019-0176-0>>.

Lai, Y.C., Deng, J., Liu, R., Hsiao, Y.C., Zhang, S.L., Peng, W., Wu, H.M., Wang, X. and Wang, Z.L., 2018. Actively Perceiving and Responsive Soft Robots Enabled by Self-Powered, Highly Extensible, and Highly Sensitive Triboelectric Proximity- and Pressure-Sensing Skins. *Advanced Materials*, 30(28), pp.1–12.

Li, H., Yao, J., Zhou, P., Chen, X., Xu, Y. and Zhao, Y., 2020. High-force soft pneumatic actuators based on novel casting method for robotic applications. *Sensors and Actuators, A: Physical*, [online] 306, p.111957. Available at: <<https://doi.org/10.1016/j.sna.2020.111957>>.

Lipson, H., 2014. Challenges and Opportunities for Design, Simulation, and Fabrication of Soft Robots. *Soft Robotics*, 1(1), pp.21–27.

Rus, D. and Tolley, M.T., 2015. Design, fabrication and control of soft robots. *Nature*, 521(7553), pp.467–475.

Salem, M.E.M., Wang, Q., Wen, R. and Xiang, M., 2018. Design and Characterization of Soft Pneumatic Actuator for Universal Robot Gripper. In: *2018 International Conference on Control and Robots, ICCR 2018*. IEEE, pp.6–10.

She, Y., Li, C., Cleary, J. and Su, H.J., 2015. Design and fabrication of a soft robotic hand with embedded actuators and sensors. *Journal of Mechanisms and Robotics*, 7(2), pp.1–9.

Su, Y., Zhu, G., Yang, W., Yang, J., Chen, J., Jing, Q., Wu, Z., Jiang, Y. and Wang, Z.L., 2014. Triboelectric sensor for self-powered tracking of object motion inside tubing. *ACS Nano*, 8(4), pp.3843–3850.

Sun, T., Chen, Y., Han, T., Jiao, C., Lian, B. and Song, Y., 2020. A soft gripper with variable stiffness inspired by pangolin scales, toothed pneumatic actuator and autonomous controller. *Robotics and Computer-Integrated Manufacturing*, 61(August 2019).

Sun, Y., Song, Y.S. and Paik, J., 2013. Characterization of silicone rubber based soft pneumatic actuators. *IEEE International Conference on Intelligent Robots and Systems*, pp.4446–4453.

Wakimoto, S., Suzumori, K. and Ogura, K., 2011. Miniature pneumatic curling rubber actuator generating bidirectional motion with one air-supply tube. *Advanced Robotics*, 25(9–10), pp.1311–1330.

Wang, S., Lin, L. and Wang, Z.L., 2015. Triboelectric nanogenerators as self-powered active sensors. *Nano Energy*, 11, pp.436–462.

Wang, Z., Or, K. and Hirai, S., 2020. A dual-mode soft gripper for food packaging. *Robotics and Autonomous Systems*, [online] 125, p.103427. Available at: <<https://doi.org/10.1016/j.robot.2020.103427>>.

Wang, Z., Zhu, M., Kawamura, S. and Hirai, S., 2018. Fabrication and performance comparison of different soft pneumatic actuators for lunch box packaging. *2017 IEEE International Conference on Real-Time Computing and Robotics, RCAR 2017*, 2017-July, pp.22–27.

Wang, Z.L., Lin, L., Chen, J., Niu, S. and Zi, Y., 2016. Triboelectricification. In: *Triboelectric Nanogenerators*. Springer, Cham. pp.1–19.

Yap, H.K., Ng, H.Y. and Yeow, C.H., 2016. High-Force Soft Printable Pneumatics for Soft Robotic Applications. *Soft Robotics*, 3(3), pp.144–158.

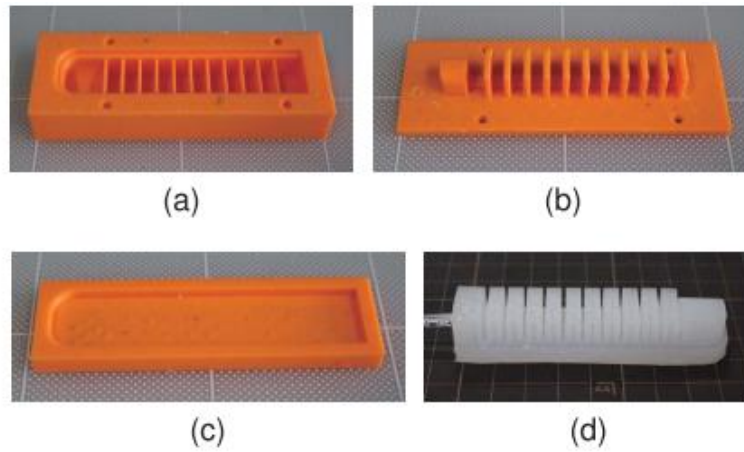
Zhong, G., Hou, Y. and Dou, W., 2019. International Journal of Mechanical Sciences A soft pneumatic dexterous gripper with convertible grasping modes.

International Journal of Mechanical Sciences, [online] 153–154(February), pp.445–456. Available at: <<https://doi.org/10.1016/j.ijmecsci.2019.02.028>>.

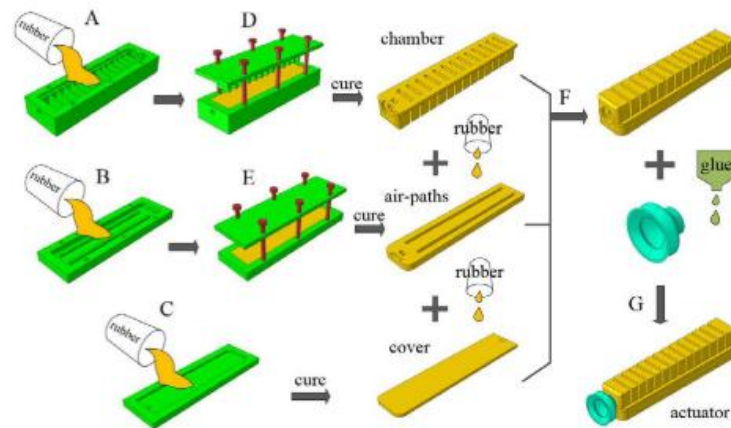
Zhu, M., Xie, M., Lu, X., Okada, S. and Kawamura, S., 2020. Nano Energy A soft robotic finger with self-powered triboelectric curvature sensor based on multi-material 3D printing. *Nano Energy*, [online] 73(April), p.104772. Available at: <<https://doi.org/10.1016/j.nanoen.2020.104772>>.

APPENDICES

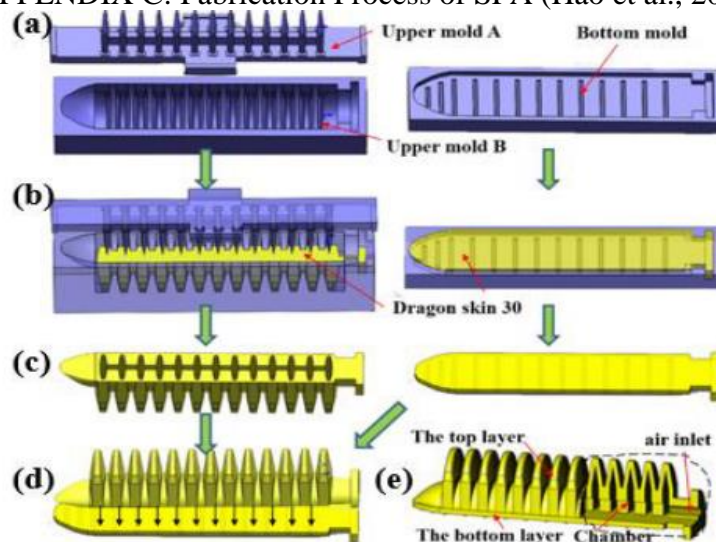
APPENDIX A: Fabrication Process of SPA (Wang, et al., 2017)



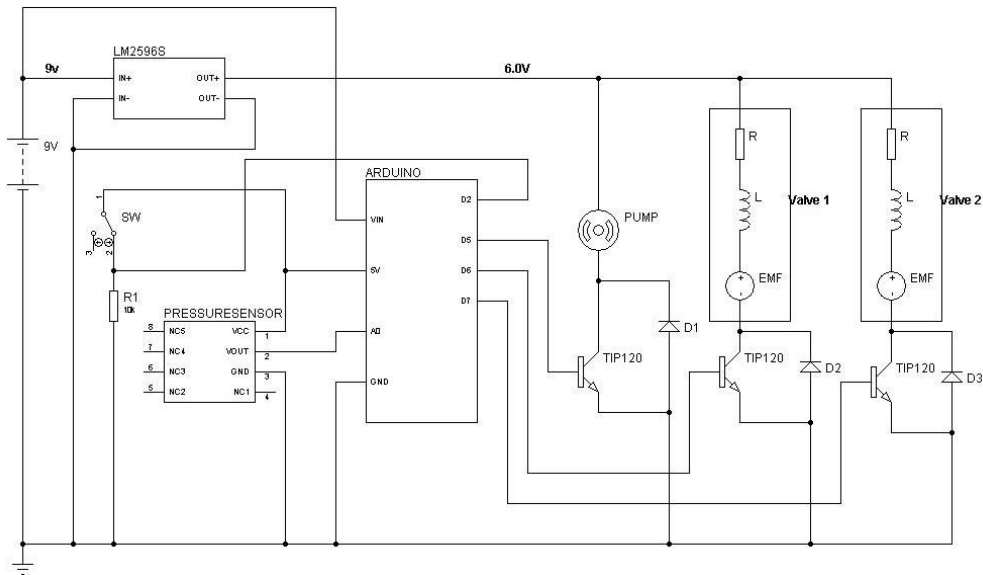
APPENDIX B: Fabrication Process of SPA (Wang, Or amd Hirai, 2020)



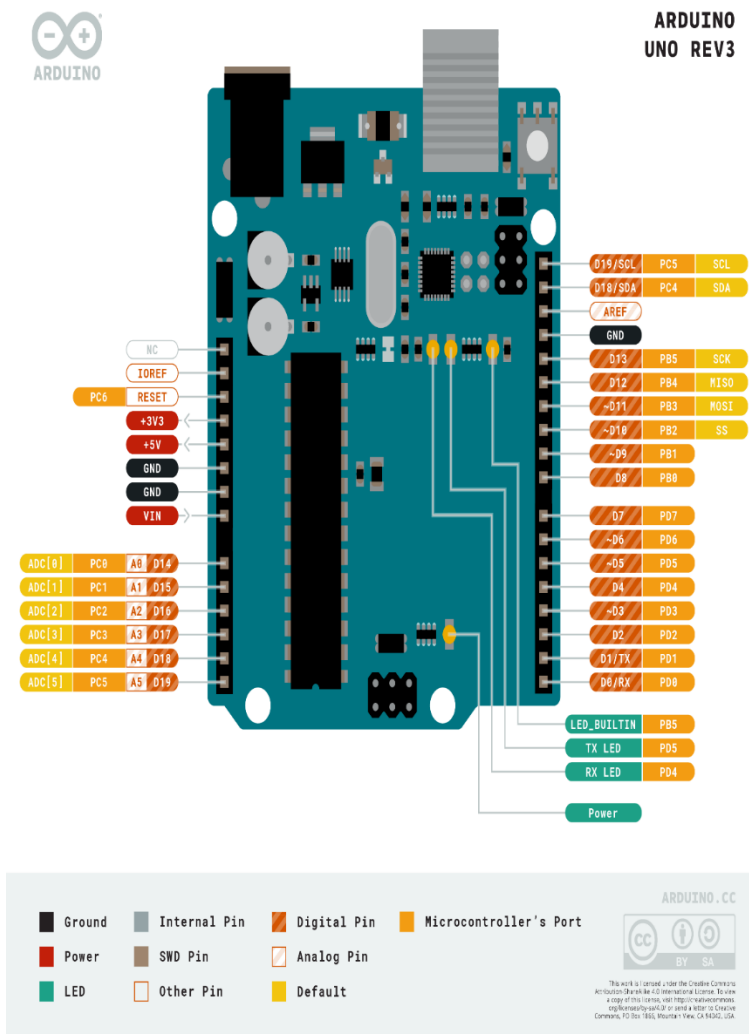
APPENDIX C: Fabrication Process of SPA (Hao et al., 2016)



APPENDIX D: Pneumatic Circuit Diagram (Soft Robotic Toolkit, 2020)

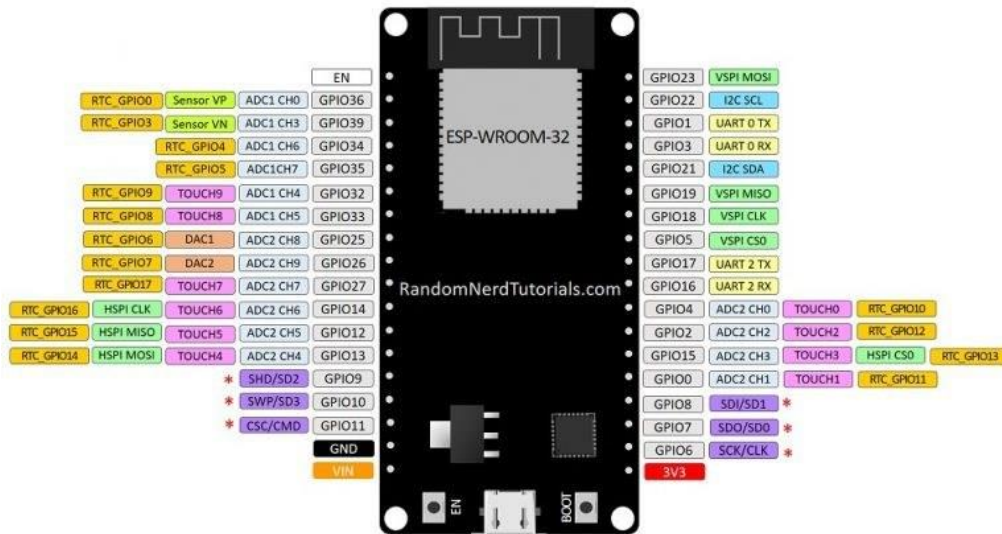


APPENDIX E: Pinout Diagram of Arduino UNO R3 (Arduino, 2020)



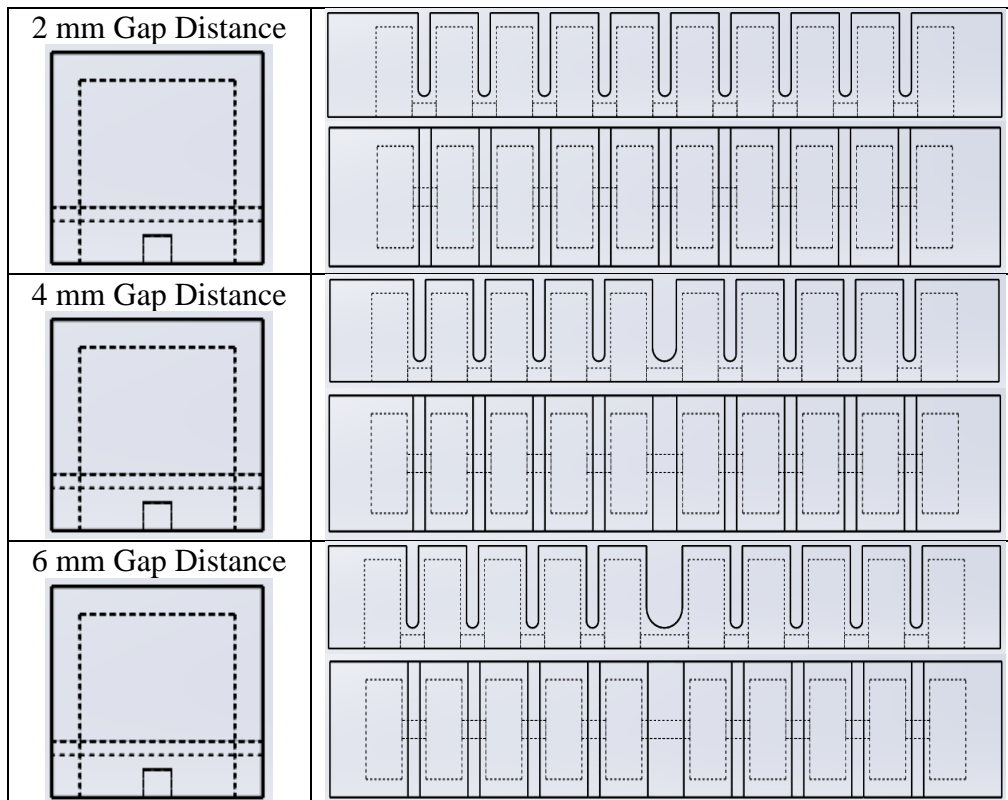
APPENDIX F: Pinout Diagram of ESP32 (Random Tutorials, n.d.)

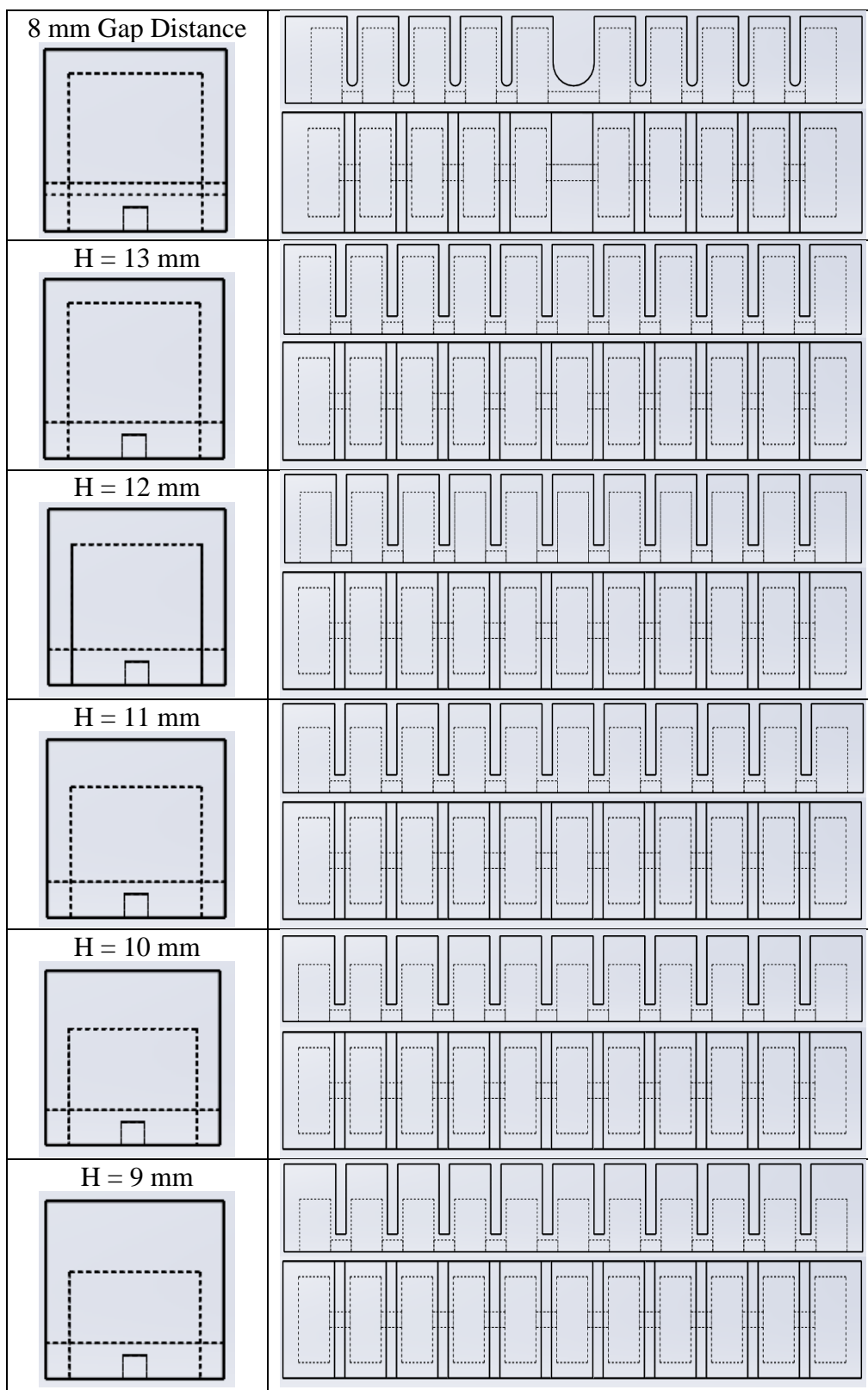
ESP32 DEVKIT V1 - DOIT
version with 36 GPIOs

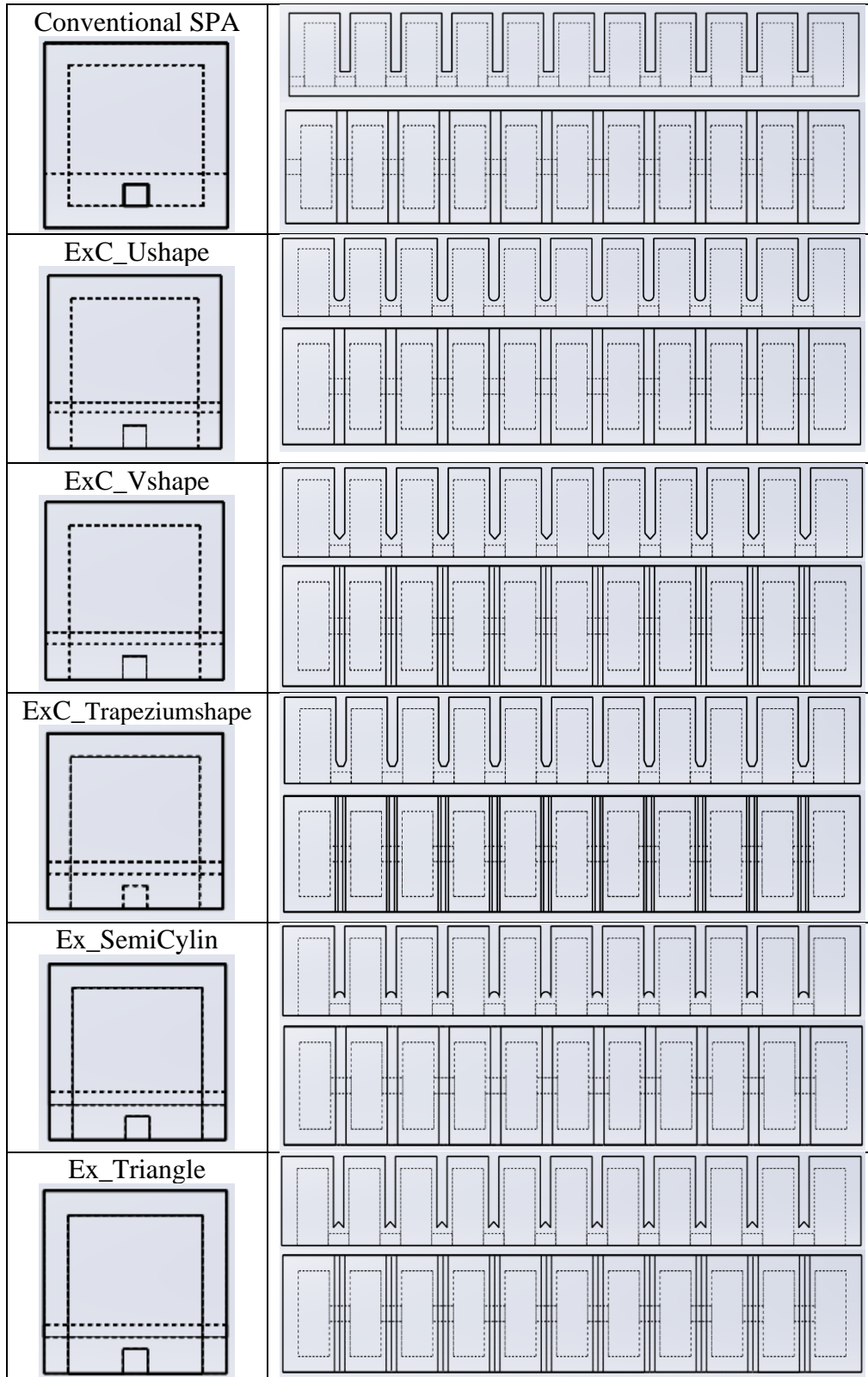


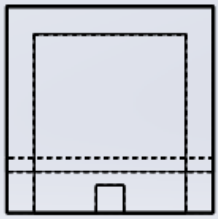
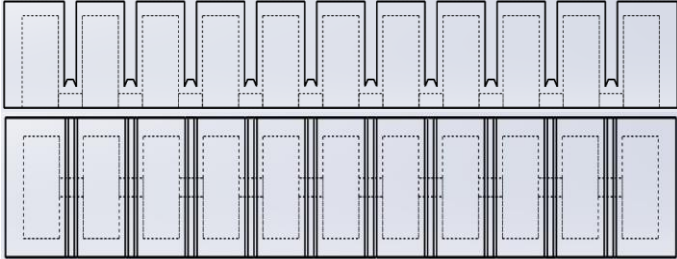
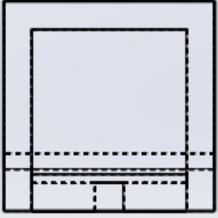
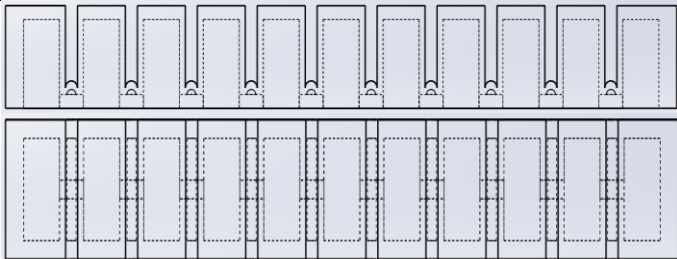
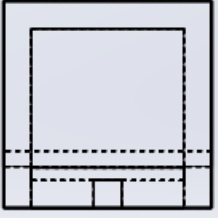
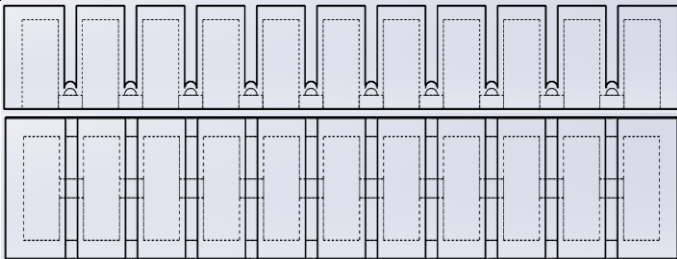
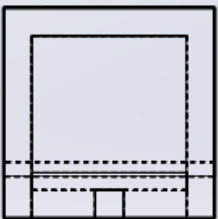
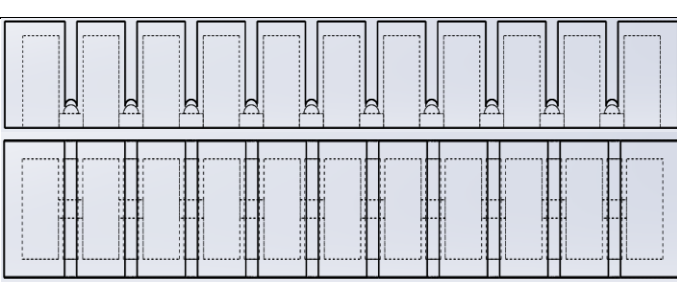
* Pins SCK/CLK, SDO/SD0, SDI/SD1, SHD/SD2, SWP/SD3 and SCS/CMD, namely, GPIO6 to GPIO11 are connected to the integrated SPI flash integrated on ESP-WROOM-32 and are not recommended for other uses.

APPENDIX G: Design of all SPA







<p>Ex_Trapezium</p>  <p>A cross-sectional diagram of a trapezoidal structure. It features a central rectangular area with a dashed border. Below this area, there is a horizontal dashed line, and further down, a solid horizontal line with a small rectangular protrusion centered underneath it.</p>	 <p>Two views of the Ex_Trapezium structure. The top view shows a row of ten trapezoidal shapes with semi-cylindrical protrusions on their top surfaces. The bottom view shows a row of ten rectangular shapes with vertical lines and horizontal dashed lines, representing the internal structure or assembly points.</p>
<p>1.5 mm semi cylin air chamber</p>  <p>A cross-sectional diagram of a structure with a 1.5 mm semi-cylindrical air chamber. It features a central rectangular area with a dashed border. Below this area, there is a horizontal dashed line, and further down, a solid horizontal line with a semi-cylindrical protrusion centered underneath it.</p>	 <p>Two views of the 1.5 mm semi-cylindrical air chamber structure. The top view shows a row of ten trapezoidal shapes with semi-cylindrical protrusions on their top surfaces. The bottom view shows a row of ten rectangular shapes with vertical lines and horizontal dashed lines.</p>
<p>2.0 mm semi cylin air chamber</p>  <p>A cross-sectional diagram of a structure with a 2.0 mm semi-cylindrical air chamber. It features a central rectangular area with a dashed border. Below this area, there is a horizontal dashed line, and further down, a solid horizontal line with a semi-cylindrical protrusion centered underneath it.</p>	 <p>Two views of the 2.0 mm semi-cylindrical air chamber structure. The top view shows a row of ten trapezoidal shapes with semi-cylindrical protrusions on their top surfaces. The bottom view shows a row of ten rectangular shapes with vertical lines and horizontal dashed lines.</p>
<p>Improved SPA 2.5 mm semi cylin air chamber</p>  <p>A cross-sectional diagram of a structure with a 2.5 mm semi-cylindrical air chamber. It features a central rectangular area with a dashed border. Below this area, there is a horizontal dashed line, and further down, a solid horizontal line with a semi-cylindrical protrusion centered underneath it.</p>	 <p>Two views of the Improved SPA 2.5 mm semi-cylindrical air chamber structure. The top view shows a row of ten trapezoidal shapes with semi-cylindrical protrusions on their top surfaces. The bottom view shows a row of ten rectangular shapes with vertical lines and horizontal dashed lines.</p>

APPENDIX H: Pressure Table Generated by MPX5500DP

Syringe (ml)	Pressure (kPa)					
	Trial 1	Trial 2	Trial 3	Trial 4	Trial 5	Average
2.9	4.37	5.45	4.91	4.51	4.82	4.81
3.0	6.00	6.00	6.00	6.00	6.00	6.00
3.1	6.54	6.27	6.27	6.27	6.00	6.27
3.2	7.08	7.08	7.62	7.35	7.76	7.38
3.3	8.17	8.30	8.17	8.44	8.17	8.25
3.4	10.34	10.34	9.93	10.34	9.80	10.15
3.5	12.51	12.51	11.42	12.51	12.81	12.35
3.6	14.68	13.73	13.87	14.14	14.14	14.11
3.7	15.76	15.22	16.49	15.49	15.22	15.64
3.8	17.94	17.39	17.12	16.85	17.12	17.28
3.9	18.48	17.66	18.21	18.48	17.94	18.15
4.0	20.11	20.38	21.19	20.11	20.10	20.38
4.1	22.28	21.73	21.87	21.73	21.46	21.81
4.2	23.36	23.36	24.45	23.63	24.04	23.77
4.3	24.72	24.45	24.04	24.45	24.18	24.37
4.4	26.21	26.08	25.80	25.53	25.53	25.83
4.5	27.70	27.70	27.97	27.70	27.70	27.75
4.6	29.87	29.87	28.79	29.87	28.92	29.46
4.7	30.15	30.55	30.15	30.42	30.28	30.31
4.8	31.64	31.23	31.09	31.50	30.96	31.28
4.9	32.32	32.59	32.04	32.32	32.72	32.40
5.0	34.76	34.89	34.22	34.49	34.35	34.54
5.1	36.39	35.84	35.84	35.44	35.57	35.82
5.2	37.61	38.01	37.88	37.47	37.47	37.69
5.3	39.10	39.91	39.91	39.23	39.37	39.50
5.4	40.86	40.73	40.73	41.00	40.46	40.76
5.5	43.58	43.98	43.98	43.44	43.03	43.60
5.6	45.07	44.53	44.53	44.12	44.25	44.50
5.7	46.15	47.92	49.41	47.78	48.05	47.86
5.8	51.04	51.88	50.77	50.50	49.68	50.77
5.9	52.94	53.21	52.80	53.75	52.12	52.96
6.0	55.92	55.92	55.11	55.92	54.84	55.54

APPENDIX I: Triboelectric Series (Diaz and Felix-Navarro, 2004)

Comparison of four published triboelectric series			
Ref. [3]	Ref. [4]	Ref. [5]	Ref. [6]
Positive charge			
		Silicone elastomer with silica filler	Air
		Borosilicate glass, fire polished	Human hands ←
	Wool	Window glass	Asbestos
		Aniline-formol resin	Rabbit fur
		Polyformaldehyde	Glass
		<i>Polymethyl methacrylate</i>	Mica
		Etylcellulose	Human hair
		Polyamide 11	
Nylon 6,6	Nylon	Polyamide 6-6	Nylon
		Rock salt (NaCl)	Wool
		Melanime formol	Fur
		Wool, knitted	Lead
		Silica, fire polished	Silk
	Viscose	Silk, woven	Aluminum ←
Cellulose		Polyethylene glycol succinate	Paper
Cellulose acetate		Cellulose acetate	
		Polyethylene glycol adipate	
		Polydiallyl phthalate	
		Cellulose (regenerated) sponge	
	Cotton	Cotton, woven	Cotton
		Polyurethane elastomer	Steel
	Silk	Styrene-acrylonitrile copolymer	Wood
		Styrene-butadiene copolymer	Amber
	Acetate	Polystyrene	Sealing wax
Polymethyl methacrylate	Lucite	Polyisobutylene	Hard rubber
Polyacetate	Polyvinyl alcohol	Polyuretane flexible sponge	Nickel, Copper
	Dacron	Borosilicate glass, ground state	Brass, Silver
Polyethylene terephthalate		Polyethylene glycol terephthalate	Gold, Platinum
		Polyvinyl butyral	Sulfur
		Formo-phenolique, hardened	Acetate, Rayon
		Epoxide resin	Polyester
		Polychlorobutadiene	Styrene (Styrofoam)
	Orlon	Butadiene-acrylonitrile copolymer	Orlon
		Natural rubber	
Polyacrylonitrile		Polyacrilonitrile	Saran
<i>Polyvinyl chloride</i>	<i>Polyvinyl chloride</i>	Sulfur	
Polybisphenol carbonate	Dynel		
Polychloroether	Velon		Polyurethane
Polyvinylidene chloride			
Poly(2,6-dimethyl polyphenylene oxide)			
<i>Polystyrene</i>			
<i>Polyethylene</i>	<i>Polyethylene</i>	Polyethylene	Polyethylene ←
<i>Polypropylene</i>		Polydiphenylol propane carbonate	Polypropylene ←
		Chlorinated polyether	
		Polyvinyl chloride with 25% DOP	Vinyl (PVC)
		Polyvinyl chloride without plasticizer	Silicon ←
		Polytrifluoroethylenoethylene	
		Polytetrafluoroethylene	Teflon
		Polytetrafluoroethylene	Teflon
Negative charge			

APPENDIX J: Arduino Code (Main Program)

```
#include <Wire.h>

#include <Adafruit_GFX.h>

#include <Adafruit_SSD1306.h>

#define ExtendButton 26 //purple cable

#define RetractButton 25 //blue cable

#define MotorPin1 13 //white cable

#define MotorPin2 12 //grey cable

#define SCREEN_WIDTH 128 // OLED display width, in pixels
#define SCREEN_HEIGHT 64 // OLED display height, in pixels
// Declaration for an SSD1306 display connected to I2C (SDA, SCL pins)
Adafruit_SSD1306 display(SCREEN_WIDTH, SCREEN_HEIGHT, &Wire, -1);

String motorcond;//for OLED display motor condition
unsigned long time_extend; //for millis() function
unsigned long time_retract; //for millis() function
//unsigned long time_test; //for millis() function

void setup() {
  pinMode(ExtendButton, INPUT); //initialize input for Inflate push button
  pinMode(RetractButton, INPUT); //initialize input for Deflate push button
  pinMode(MotorPin1, OUTPUT); //initialize output for Motor driver pin1
  pinMode(MotorPin2, OUTPUT);
  Serial.begin(115200);
  display.begin(SSD1306_SWITCHCAPVCC, 0x3C); //update OLED
  delay(4000);
}
```

```
void loop() {  
  //for extend//inflate  
  if((digitalRead(ExtendButton)==LOW)&&(digitalRead(RetractButton)==HIGH)){  
  
    time_extend=millis();  
    while (millis()-time_extend<=1600){ //extend for n seconds, can be adjusted  
      motorcond = "Retract";  
      display_OLED();  
      digitalWrite(MotorPin1, LOW); //to deflate  
      digitalWrite(MotorPin2, HIGH);  
      delay(200); //adjust how long you want to it retract  
      motorcond = "Delay";  
      display_OLED();  
      digitalWrite(MotorPin1, LOW); //Pause for awhile  
      digitalWrite(MotorPin2, LOW);  
      delay(800); //adjust how long you want to it delay  
      motorcond = "Extend";  
      display_OLED();  
      digitalWrite(MotorPin1, HIGH); //to inflate  
      digitalWrite(MotorPin2, LOW);  
      delay(600); //adjust how long you want it to extend  
    }  
  }  
}
```

```

//for retract//deflate
if((digitalRead(RetractButton)==LOW)&&(digitalRead(ExtendButton)==HIGH)){
    time_retract=millis();
    while (millis()-time_retract<=400){//extend for n seconds, can be adjusted
        motorcond = "Retract";
        display_OLED();
        digitalWrite(MotorPin1, LOW);    //back to initial position
        digitalWrite(MotorPin2, HIGH);
        delay(400);            //adjust how long you want to it retract
    }
}

//for off status

if(((digitalRead(RetractButton)==HIGH)&&(digitalRead(ExtendButton)==HIGH))| |((digitalRead(RetractButton)==LOW)&&(digitalRead(ExtendButton)==LOW))){
    digitalWrite(MotorPin1, LOW);
    digitalWrite(MotorPin2, LOW);
    motorcond = "Off";
    display_OLED();
}

}

void display_OLED(){
    display.clearDisplay(); // Clear display
    display.setTextSize(2);
    display.setTextColor(WHITE);
    display.setCursor(0,0);
    display.print("Status: ");
    display.setTextSize(3);
    display.setCursor(0,30);
    display.print(motorcond);
    display.display();
}

```


APPENDIX K: Arduino Code (MPX5500DP Pressure Sensor)

```
#include <Wire.h>

#include <Adafruit_GFX.h>

#include <Adafruit_SSD1306.h>

const int Sensor = 34;

int SensorValue = 0;

void setup() {
  Serial.begin(115200);
}

void loop() {
  SensorValue=analogRead(Sensor); //read the analog value between 0 to 4095
  if(SensorValue!=0){
    float SensorVoltage=SensorValue*(3.3/4095); //what is the voltage in 3.3
    float toFiveVolt = SensorVoltage *(5/3.3); //convert it back to 5V analog in value
    float kPa = (toFiveVolt-0.2)/0.009; //formula from datasheet
    Serial.println("Raw Value is = ");
    Serial.print(SensorValue);
    Serial.println();
    Serial.println("in kPa is = ");
    Serial.print(kPa);
    Serial.println();
    Serial.println();
    delay(1000);
  }
}
```